Structure and Deformation of the Sudbury Impact Crater

A Thesis

Submitted to the School of Geography and Earth Sciences

In Partial Fulfillment of the Requirements

For the Degree

Master of Science

McMaster University

MASTER OF SCIENCE (2011) McMaster University

School of Geography and Earth Sciences Hamilton, Ontario

TITLE: Structure and Deformation of the Sudbury Impact Crater

SUPERVISOR: W. A. Morris

List of Tables

List of Figures

Abstract:

Digital elevation models (DEM) can be used for a multitude of applications. Under ideal circumstances, calibration of a remotely acquired estimate of topographic elevation is calibrated through use of ground control points (GCP) which would be ubiquitous, seamlessly joining remotely sensed data and high accuracy check points. In reality there are many areas on the earth's surface which are difficult, expensive, or dangerous to access. Under these circumstances, the acquisition of GCPs may not be realistic and relative DEMs must be used. Innovative methods must then be used to determine the relative error associated with a DEM in a given study area. The method presented in this paper compares three DEMs (ASTER, CDED, SRTM) derived from independent acquisition systems to determine their relative errors.

The ASTER DEM data was chosen for a lineament analysis study in north central Ontario, Canada. This study used a quantitative digital approach to determine the density of lineaments mimicking the geometry of the northern Sudbury Igneous Complex contact (SIC). The study revealed a lineament density at ~25km north of the northern SIC contact, suggesting a ring structure from an ancient multi-ring impact basin. This argument is supported by findings of the pattern of plagioclase clouding intensities in Matachewan dykes in the vicinity of the ring structure. The orientation of the dykes may have some connection to the faulting and block rotation caused by crater wall collapse.

Paleomagnetic data from the norite in the SIC and Foy Offset dyke combined with an unconstrained magnetic inversion of the Foy Offset dyke suggest that the Sudbury Structure has not been folded, but instead has been deformed by brittle deformation.

Acknowledgements:

First and foremost I would like to thank my supervisor Dr. Bill Morris for the innumerable hours he spent helping bringing this project into fruition.

I would like to thank Dr. Maureen Padden and Dr. Alan Dickin for their thoughtful comments on my project.

I would also like to thank my family Sally MacDonald, John Underhay, Josh Underhay and Mitchell Underhay for providing constant support throughout my degree.

Vicki and Peter Tschirhart, Madeline Lee and Bill Spicer deserve many thanks for the encouragement they provided me over the years.

Chapter 1

Introduction

Although Dietz (1964) first suggested an impact origin for the Sudbury Igneous Complex (SIC) in 1964, it took over forty years for the scientific community to come together on a revolutionary model for the original morphology of the Sudbury Impact Crater. The discovery in 1994 by Hayden Butler of groupings of linear features mimicking the geometry of the northern SIC contact provided the first evidence for potentially the largest of all terrestrial craters: the multi-ring basin (Butler, 1994). He definitively mapped one ring at about 25km north of the SIC contact and was confident enough about the presence of four other rings that he used mathematical interpolation based on the proportions of lunar craters to estimate their diameters. Other impact related features in the surrounding region support a crater of up to 270km in diameter.

Based on geological and geophysical studies, the crater was interpreted to have been initially circular and subsequently deformed (Morris, 2002). Interpolations of its original diameter have put it at anywhere between 180 km and 270 km, making it one of the largest impact craters on earth on par with Vredefort in South Africa, and Chixculub in the Yucatan Peninusula. Post-impact intense deformation of the Sudbury Structure (SS) has made it difficult to determine the exact size and morphology of the original crater. Currently, field mapping suggests that the geological contact with the North Range portion of the impact structure, which is sitting on the Archean age Levack Gneiss Complex (LGC) dip at approximately 35^{o} to the South –East (Dreuse et al., 2010). Seismic imaging collected along a basin-crossing transect as part of the Lithoprobe program suggests that the North Range continues at depth to the SE under the South Range (Deutsch, 1994). Geological mapping and seismic imaging reveal that the South Range has near vertical dips and is locally overturned (Riller et al., 1999). Detailed structural mapping and seismic imagery shows that the South Range is segmented at depth by a number of sub-parallel, shallow, south-dipping thrust surfaces collectively defined by the term South Range Shear Zone (Shanks and Schwerdtner, 1991; Dubois and Benn, 2003; Riller, 2005).

The observed geometry of the SIC can be explained in two ways: (1) folding into a south-west plunging synformal structure accompanied by northward thrusting along the South Range Shear Zone (Shanks and Schwerdtner, 1991; Riller 2005); or (2) northward directed thrusting and slab rotation (Morris, 2002). If the current morphology of the Sudbury Structure is to be explained by folding along an NE/SW trending axis one might expect that there should be some

vestige of the folding in the rocks immediately underlying the current North Range contact. Alternatively, if the current geometry of the Sudbury Structure is explained in terms of a series of south-dipping thrust slices then there is no requirement for continuity of tectonic deformation from the area of the SIC to the surrounding region. Rather each slab could contain only syn-impact deformation which would exhibit a pattern that is coherent with the SIC contact.

In order to study the remains of the outer limits of this basin, one must differentiate between orogenic and impact related artifacts. This area has experienced a number of temporally distinct geological events, for example there have been at least three orogenic events that could have caused faulting in the Superior Province. The Blezardian Orogeny is thought to have occurred 2.4- 2.2Ga, the 1.89-1.83 Ga Penokean Orogeny and the 1.12-0.98 Ga Grenville Orogeny (Riller et al., 1999; Carr et al., 2000).

Three swarms of dikes have been mapped within the study area; 2.47 Ga Matachewan dykes, ~2.2 Ga Nippissing sills, and 1.24 Ga of the Sudbury dykes (Siddorn, 2002). There are numerous fracture patterns in the study area that cannot be definitively associated with any of the known orogenic events. Analysis of their patterns will help determine if they are instead associated with the Sudbury impact crater.

This study focuses on evidence for the existence and locus of the third of Butler's rings. Results are derived from a quantitative investigation of the spatial distribution of valleys and depressions present in the digital topographic record. Topography is represented in Digital Elevation Models (DEM) derived from both satellite and airborne systems. An analysis of three DEMS (the Advanced Space-born Thermal Emissions Reflection Radiometer, ASTER, the Canadian Digital Elevation Database, CDED, and the Shuttle Radar Topography Mission, SRTM)) was undertaken to determine the appropriateness of the DEMs to the study area.

The depth of emplacement of Matachewan dykes using plagioclase clouding indicators, and Matachewan dyke azimuth further support the presence of a down faulted block ~25km north of the SIC contact. Magnetic inversion modeling of the Foy Offset dyke and paleomagnetic results from previous studies (Sopher, 1963; Larochelle, 1969; Morris, 1982; Morris and Pay, 1981; Szabo and Halls, 2006) along with the well-defined and undeformed crater ring suggests brittle deformation of the SIC and the surrounding areas.

Chapter 2

Mapping errors associated with Digital Elevation Models ASTER, SRTM & CDED; A case study from Northern Ontario.

Introduction

Digital Elevation Models (DEM) are becoming increasingly important in geological and geomorphological studies around the world as is reflected by introduction of the term geomorphometry (Pike, 2002) to reflect quantitative analysis of topographic surfaces. There are two ways to regard the shape of the earth's surface which are divided into elevation models and terrain models. DEMs represent the ground surface elevation above sea level. The Digital Terrain Models (DTM) describe the upper envelope of all features on the earth's surface; locally this could include all natural and manmade infrastructures while at other points it might be the elevation surface. Due to the demand for increasing resolution in DEMs and DTMs, several different acquisition systems have been developed to maximize our ability to map features such as high latitude, steep slopes, canopy cover, and flat terrain.

Elevation information can be acquired from four different methods (Bossler et al., 2002, Ch. 10).

1) **In situ measurements**: using traditional surveying methods or modern GPS technologies, these methods can produce very accurate x,y,z positions but are labor intensive, time consuming and are often difficult to obtain in areas of dense vegetation cover.
2) **Stereo - Photogrammetry:** uses the principals of stereoscopic visualization to obtain local point estimates of x, y, z information over large geographical area. While initially applied to aerial photographic surveys which are based on overlapping photographic pairs, the advent of satellite systems now provides optical imagery with dual look direction. Stereo-photogrammetry has now been extended to include satellite data.

3) **SPOT and ASTER**, (Mitchell, 2011): This method can yield a high resolution DEM for inhospitable terrain but is unable to provide information on the topographic surface in areas with dense vegetation or where dense cloud cover limits visibility of the earth surface.
4) **Interferometric Synthetic Aperture Radar (INSAR):** is an active sensor which uses the principal of phase differences between radar signals to determine the x, y, z information for a given point on the earth's surface. This method produces very accurate measurements with spatial resolution being dependent on factors such as the wavelength of the transmitted signal, and the details of the receiver configuration. While radar methods are capable of penetrating clouds they cannot penetrate snow and vegetation cover (Farr, 2007).
5) **Light Detection and Ranging (LIDAR):** uses the double travel time of optical lasers to determine the elevation of the ground surface. Initially LIDAR systems used only the first arrival information, but more recently developed systems that record a full waveform which makes it possible to differentiate between bare earth ground elevation data and vegetative cover (Jensen, 2007).

Ideally, for the same area each of these systems should provide the same elevation surface. However, the four technologies are based on different types of sensors and are processed using different interpretation algorithms. This paper compares three elevation data acquisition systems: the Canadian Digital Elevation Data (CDED) based on photogrammetry using aerial photography, the Advanced Space-borne Thermal Emissions and reflection Radiometer (ASTER) based on satellite derived optical imagery, and the Shuttle Radar Topography Mission (SRTM) which used a special shuttle based radar (INSAR) configuration. With each of these

technologies using different acquisition and processing techniques, each possesses individualized advantages and disadvantages which have resulted in slightly different DEMs. Being aware of the types of errors and discrepancies between datasets is important in assigning accuracy to any subsequent use of the DEMs.

With the availability of DEM datasets and their increasing popularity as a tool in earth science applications, a detailed understanding of their capabilities and limitations is essential to proper use and extract the best possible data. This study will focus on an area of geological interest, on the boundary between the Superior and the Southern Provinces in central Ontario. With little outcrop available due to dense vegetation cover, direct geological measurements are difficult to obtain. Innovative methodologies to determine the geological history of the area are required. This study area is riddled with faults and fractures which tend to develop into topographic lows. By processing a DEM, these areas of interest can be enhanced and studied. To satisfactorily accept the results it is essential to know what is being measured and at what resolution (Toutin, 2002). This will allow for more accurate error estimates on the results. This study will compare ASTER, CDED and SRTM data for their resolution, differences in vegetation penetration ability, slope viewing, and acquisition errors to give the reader the tools they will require to further study this area or the basis to build on similar principals in other areas.

Study Area

The study area is a 140 km by 110 km region of the Superior Province in central Ontario, northwest of Sudbury (Figure 2.1). Geologically the terrain is composed mostly of granite and gneiss and has a relief of between 350m and 450m with a mean elevation of about 415m above

sea level. In the southeast corner of the study area lies the 1.85 Ga Sudbury Igneous Complex (SIC) (Halls, 2009) surrounded to the north by the 2.71 Ga ± 0.007 Ga (Krogh et al., 1984) Levack Gneiss Complex. Radiating northwest from the SIC is the Foy offset dike associated with the crater melt (Lightfoot, 1997). Swarms of 1.25 Ga olivine diabase dikes trending WNW and 2.45 Ga Matachewan dikes trending NNW cross most of the study area.

Data Sources

CDED System

The Canadian Digital Elevation Data (CDED) is a digital compilation of the topographic maps from the National Topographic System (NTS). It is a series of evenly distributed elevation points with a north-south resolution of ~23m and east-west resolution of 11 to16m and a vertical error of ~20m as defined for the study area in this project. The original images were obtained from airborne photography that was acquired between 1990 and 1993 and subsequently translated into digital topographic information via photogrammetry (Gov. Can., 2000).

Photogrammetry is the extraction of real world spatial measurements from air photographs (Jensen, 2007). To obtain coverage of an area of interest, an aircraft would fly a series of closely spaced transects (flight lines) while taking photographs of the land below. Each photograph is a simple image of the instantaneous ground cover under the aircraft. Any clouds, vegetation, or snow cover between the ground surface and the camera at the time of image acquisition would preclude using that area to obtain meaningful topographic information. A mosaic of images for a given area is created by overlapping each successive photograph along a flight line by 60% and by 20-30% between each flight line. This overlap allows each ground

point to be covered by at least two and sometimes three photographs from various angles. Using several vantage points to view a single object with height allows us to use the principals of stereoscopic parallax to derive the elevation of said point. Stereoscopic parallax is defined as "the change in position of an object with height, from one photograph to the next relative to its background, caused by the aircrafts motion" (Jensen, 2007). Determining the height of an object using stereoscopic photogrammetric techniques requires that: (1) the photographs must have been acquired within 3° of vertical, (2) adjacent photographs are acquired at the same altitude, (3) the principal points and the object of interest of adjacent photographs must be acquired at the same altitude (Jensen, 2007).

ASTER System

The Advanced Spaceborne Thermal Emissions and Reflection Radiometer (ASTER) is one of five remote sensing systems aboard the Terra satellite. Created as a joint project between the National Aeronautics and Space Administration (NASA) and Japan's Ministry of International Trade and Industry, it was launched in December 1999. The Terra satellite revolves around the earth at a height of 705km following a sun-synchronous orbit with an orbital inclination of 98.3° from the equator, an orbit period of 98.88 minutes and a ground track repeat cycle of 16 days. With a swath width of 60m, using a whisk broom scanning system, ASTER achieved a resolution of "20m at 95% confidence for vertical and 30m at 95% confidence for horizontal" (ASTER GDEM validation, 2009; Hirano et al, 2003). The terrain elevation information is obtained at 30m spacing by automated stereoscopic correlation of the images obtained from the two telescopes (one is nadir looking forward and the other is looking looking at 27.7° off nadir) aboard the ASTER system (Lillesand and Kiefer, 2000).

The photogrammetric method used alone is incapable of estimating the absolute elevation above sea level and instead produces a relative elevation model. Conversion from a relative reference frame to an absolute geographical reference frame requires the use of ground control points (GCP). These control points are obtained by in-situ field measurements using either GPS or leveling from known bench marks. Critical to this reference is the number and distribution of GCPs. For areas of limited, or smoothly grading topographic relief it may be possible to derive a reasonable DEM with a limited number of GCPs. However, in regions with strong and rapidly changing topographic relief ideally one should have one or more GCPs per individual photographic image. Such a situation is rarely achieved since acquisition of individual GCPs is limited by issues such as accessibility, or poor satellite communication.

In June 2009 the ASTER Global DEM Validation Summary Report was released by the ASTER GDEM Validation team: METI/ERSDAC, NASA/LPDAAC and USGS/EROS (ASTER GDEM, 2009). This report detailed the relative and absolute vertical and horizontal accuracy and errors associated with the global ASTER DEM. They compared ASTER with the National Geodetic Survey (NGS) which comprises more than 13000 GCPs, the USGS National Elevation Dataset (NED) and SRTM data. ASTER data was subtracted from each of these datasets to obtain the maximum, minimum, mean, standard deviation and RMSE for each combination set. The results showed that ASTER displayed a typical negative bias, meaning it was generally lower than its counterparts by approximately 5m. On flat surfaces this bias increased to -6.4m and in vegetated areas it decreased to + 1.7 m, since it was probably recording the canopy instead of the ground.

Errors such as step anomalies were interpreted as being created from the overlap of swath paths. Bumps and pits are randomly distributed positive and negative anomies respectively. Mole runs are positive anomalies that take the shape of some curvilinear stack number boundaries and occur primarily in flat terrain.

SRTM System

The Shuttle Radar Topography Mission (SRTM) was a joint project between NASA, the NGA (National Geospatial-Intelligence Agency of the U.S. Department of Defense) and the DLR (German Aerospace Center) to create a high-resolution high-accuracy topographic dataset covering the earth from 60° north to 58°south (Farr, 2007). The Shuttle was launched in February 2000 and completed the project in just ten days. The Shuttle had an orbital inclination of 57°, a swath width of 225km and completed 159 orbits imaging the earth's surface with a radar beam to obtain a horizontal ground resolution for the study area of 90m by 90m with an absolute height error of 9m. Since the radar beam is a controlled source with known wavelength and phase it is possible to derive high resolution distance information from phase interference between the transmitted and reflected signal. The topographic information is revealed through computation of an interferogram with progressive changes in phase cycle in the slant angle image representing a combination of topography and increasing distance from the shuttle. By systematically converting the inteferogram from slant range to ground range it is possible to extract topographic information (Massonet, 1998). Errors associated with the data acquisition can be classified into three wavelength categories: long (residual roll), medium (random) and short (speckle). All topography based on radar INSAR processing is critically dependent upon accurate knowledge of the location and orientation of the sensor platform. Unresolved changes in

platform orientation can result in apparent long wavelength topographic changes. All INSAR systems are side-looking which leads to slant range, and orientation-dependent localized distortions. Improved resolution of INSAR topography can be achieved by joint processing of radar imagery with photogrammetry derived topography. In areas with extreme elevation differences (urban areas) below the study resolution, these anomalies will skew the averaged pixel elevation (Farr et al., 2007).

Data Analysis

SRTM data was acquired through Geosofts' Oasis Montaj data seeker, CDED through GeoBase's Data download and ASTER through Earth Remote Sensing Data Analysis Center (ERSDAC) and the NASA Land Processes Distributed Active Archive Center (LP DAAC). GCPs were not obtained for this study because the desired analysis did not require absolute elevations but only relative topographic differences and so it was deemed financially inefficient and unnecessary to acquire them.

Direct comparison

To facilitate a direct comparison of the elevation described by the three data sets, each was transformed into a grid with the same spatial extent. Each data set was gridded using Geosoft's minimum curvature algorithm with a grid cell size of 20m for the ASTER and CDED data, and a 30m grid cell for the SRTM data. Each grid was referenced to a common datum and projection of WGS 1984, UTM 17N. Having a different grid cell size and a common spatial coverage, means that there are fewer pixels in the SRTM grid relative to the ASTER and CDED grids. An initial comparison between the three grids was achieved by simply computing the

maximum, minimum, mean and standard deviation. This comparison does not reveal anything about possible spatial differences in the elevation between the three grids. Spatial patterns are revealed by looking at the differences (subtraction grid) between the each of the three grids. As noted above the CDED was derived from an aerial photographic dataset which was collected along flight lines which were oriented approximately E-W. The ASTER data was collected from a sun-synchronous satellite which passed over the study area with a NNW to SSE trajectory. The INSAR Space Shuttle data also had a similar path. In order to investigate differences that might be related to individual acquisition paths we extracted two sets of profiles from the gridded data: one set of profiles is oriented parallel to the ASTER path track, while the other set of profiles is oriented perpendicular to the ASTER path track.

The azimuth and inclination of a slope in relation to the sensor, paired with the density of vegetation represent the largest error associated with these acquisition systems. Due to the nature of the study area it was not possible to entirely separate these two issues and so they must be studied simultaneously.

Slope

Slope was determined using a potential field geophysics method known as the tilt. The surface of a potential field data set is wave-like and has peaks and troughs representing geological features, very similar to a DEM data set once it is gridded and visualized. Tilt uses first derivatives of the X, Y and Z planes of the surface, be it part of the electromagnetic spectrum or a true representation of a surface to determine their rate of change. In the ASTER data, these edges represent rapid change in elevation. The total field (TF) input when using

topographic data represents the entire original dataset. The horizontal gradient magnitude (HGM) refers to the extent of change in the X, Y plane. Tilt is emphasizing the distribution of localities with steep slope. The expression below was taken from Pilkington and Keating (2004).

Total Field (TF) - Horizontal Gradient Magnitude (HGM) = $\sqrt{\left[\left\{\frac{dT}{dx}\right\}^2 + \left\{\frac{dT}{dy}\right\}^2\right]}$

Tilt = $\tan^{-1}\left\{\frac{\frac{dT}{dz}}{TF-HGM}\right\}$

The colors of the tilt grids were chosen to highlight the different slope angles (Figure 2.5). The slope grids were compared with the NDVI vegetation Landsat image (Figure 2.6) to determine areas of interest.

Depending on the look angle of the sensor system in relation to the topography, each system will have a slightly different perspective. CDED acquired data using near vertical images. When used for topographic calculations, photographic images are generally required to be within 3^o of vertical. ASTER uses two telescopes one vertical and one inclined backwards along the same track: errors in this configuration should result in differences along the flight path. In addition it should be remembered that ASTER involves a scanning mirror which oscillates perpendicular to the direction of travel: errors in this correction would produce differences parallel to the flight path. SRTM used inclined one sided sensors. In this case much depends on the orientation of the slope relative to the transmitted signal. Obviously maximum coupling occurs with slopes facing towards the signal source; the steeper the slope, the more severe the error.

Vegetation

The study area is vegetated with variable densities of boreal forest. Interspersed within this heavy forest cover are occasional rocky outcrops and large areas that have been subject to clear-cut deforestation. Limited areas are farmed and even smaller areas have been urbanized. Each of the elevation mapping techniques used in this comparison is compromised by the presence of dense vegetation cover. It is possible that some portion of each of the data actually represents canopy cover instead of ground surface. To establish any possible impact of vegetation on the elevation data we used NVDI derived from Landsat coverage of the area. The Landsat imagery used in this study was acquired during late summer and therefore represents maximum vegetation development. SRTM data was acquired during February and so snow cover is a more pertinent issue than vegetation. ASTER was acquired progressively over several years and the time of year for CDED data acquisition was not able to be determined.

As mentioned above, it was not possible to completely separate vegetation and slope, and so they were analyzed simultaneously. To determine the relationship between vegetation and elevation error eight profiles for each DEM were extracted in four combinations: Steep slope with dense vegetation, steep slope with sparse vegetation, shallow slope with dense vegetation and shallow slope with sparse vegetation. The maximum, minimum, mean, standard deviation and R^2 values were determined.

Results

As expected the three mapping methods produce broadly similar estimates of elevation (Table 2.1). The means of the three methods are within 9m, and they all have similar standard

deviation values. However, there are some notable differences when one looks at a detailed comparison between the three methods. SRTM does not detect the same maximum elevation as ASTER and CDED as it is a lower resolution and therefore does not have the high peaks and low troughs. ASTER appears to find an anomalously low minimum elevation of 105.4 above mean sea level. This result corresponds well to the average -5m relationship of ASTER to SRTM (Chrysoulakis, et. al, 2011). To accentuate similarities and differences between the various elevation models we also looked at the statistics of the difference grids (Table 2.1). While the maximum difference between the three models is quite similar the minimum and mean differences form two quite distinct groupings. Both of the difference grids which include ASTER have a mean elevation difference of -5m, and a much larger minimum difference value. The CDED-SRTM comparison has a mean elevation difference of only -0.1m. Combined, these observations are the first suggestion that perhaps there is a problem with the ASTER data.

When the CDED and SRTM grids are subtracted from the ASTER grid, as a way to determine spatial correlation, two results are visible. First, the ASTER data is predominantly lower than either the CDED or the SRTM. Second, a prominent NE-SW rectangular swath error pattern is evident in both of these difference grids (Figure 2.2). The width of each of these swath errors is approximately 20km. The form of this error appears to be a central band of predominantly positive differences bounded by a parallel but more diffuse zone with near zero (white colored) differences. In contrast, a comparison of the CDED and SRTM grids contains no large scale patterns (Figure 2.2). The spatial distribution of the error is random, and is what would be expected from different acquisition systems with different spatial resolutions. As is

shown in Figure 2.3 and 2.4, there is no increase in error when crossing this swath perpendicularly than when sampling parallel to it (Table 2.2) .

Slope and Vegetation

The results of slope and vegetation can be seen visually in Figure 2.5 & 2.6 respectively and numerically in Table 2.3. There is a variety of slope angles within the study area, the shallower slopes often correspond to denser vegetation coverage especially to the North West. Due to the similarities in data acquisition CDED and ASTER appear to respond to vegetation cover in similar ways; by mapping the canopy. In areas with low vegetation density, ASTER and CDED do not correlate well; ASTER tends to map a lower surface. SRTM did not correlate well with ASTER or CDED under any circumstance.

Discussion

In Figure 2.7a which represents the shaded gray scale ASTER DEM, a distinct linear feature is apparent and corresponds exactly with the western edge of the swath error in Figure 2.2. Figure 2.8 shows the approximate northeast- southwest swath paths of the Terra Satellite over Canada. It is therefore likely that the error seen in Figure 2.2 and Figure 2.5 correspond to a stacking error during image processing. The most straightforward method for minimizing the effect was to remove the large scale error while maintaining the details of the surface topography. This was done using various spatial filters (band pass, upward continuation, hanning window, etc.) and is effective when proper cutoffs are used.

The general trend of ASTER representing a slightly lower surface of approximately 5m is most likely due to the vegetation cover. Neither ASTER nor CDED are capable of penetrating

dense vegetation cover but ASTER is a more advanced sensor and is able to retrieve more areas of sporadic vegetation. North central Ontario is a relatively flat area covered in boreal forests and fields. Much of the relief in the landscape can be attributed to glacial carving and water flow. The amount of terrain relief is optimal for satellite sensing. As previously mentioned, in mountainous areas, the geometry of the sloping surface in relation to the sensor can cause distortions in the data. In extremely flat areas, there are no objects to compare when using stereoscopy and so can also distort the results. All of the DEMs corresponded well to each other in areas of high relief. The tendency for vegetation to grow most densely near sources of water complicates the results. Many of the areas of high relief are associated with river channels, and therefore dense vegetation. It is known from previous studies (Farr et al., 2007; Gov. Can., 2000; ASTER GDEM validation team, 2009) that none of the sensor systems used are capable of penetrating dense vegetation and so it is not surprising that all three datasets correspond relatively well in areas of dense vegetation. It is likely though that although well correlated, it does not accurately represent the ground surface.

Conclusion

ASTER, SRTM and CDED were analyzed for errors and applicability to a study area in north central Ontario. Each of the DEMs had its own set of advantages and disadvantages many of which overlapped. All three DEMs were unable to penetrate the vegetation cover and provided a variety of results due to differences in land use and time of year of acquisition. Beyond these errors ASTER also had several smaller errors associated with its image processing. The most obvious of these is the stacking error which bumps the NE-SW trending rectangular swaths up or down resulting in systematically higher or lower elevations. Smaller errors, such as moles, bumps and pits add to the irregularity of the surface.

SRTM is highly accurate in its measurements of elevation but is at a lower resolution of 90m by 90m than ASTER and CDED. Depending on the purpose of a particular study SRTM could be useful, but in an area of little relief and geologically complex structures, SRTM does not have the required resolution.

CDED has the highest resolution of all three datasets and in every case is the intermediate between ASTER and SRTM.

ASTER was chosen for further analysis in the subsequent chapters of this project. Although CDED had the highest resolution and least obvious errors, they were unknown and so unable to be accounted for. It is important to keep in mind the slight lowering in accuracy of these errors in the ASTER DEM as results for the subsequent analyses are discussed.

Digital elevation models are an extremely useful tool and new studies are constantly coming up with ways to extract even more data from them in a plethora of fields. For the accuracy of any study it is important to be aware of errors embedded in the data. GCPs should be obtained to determine the absolute error in each of the datasets. With a greater degree of certainty of the absolute elevation, further studies could be conducted to merge several DEMs into a very high resolution DEM.

References

ASTER GDEM Validation Team: METI/ERSDAC, NASA/LPDAAC, USGS/EROS, 2009. ASTER Global DEM Validation Summary Report, http://www.ersdac.or.jp/GDEM/E/image/ASTERGDEM_ValidationSummaryReport_Ver1.pdf, Date Accessed April 2011

Bossler, J.D. Jensen, J.R. McMaster, R.B. and Rizos,C., 2002. Manual of Geospatial Science and Technology, London: Taylor & Francis, 623p.

Chrysoulakis, N., Abrams, M., Kamarianakis, Y., and Stanislawski, M., 2011. Validation of ASTER GDEM for the Area of Greece. Photogrammetric Engineering & Remote Sensing, 77(2): 157-165.

Farr, T. G., Rosen, P. A., Caro, E., Crippen, R., Duren, R., Hensley, S., Kobrick, M., Paller, M., Rodriguez, E., Roth, L., Seal, D., Shaffer, S., Shimada, J., Umland, J., Werner, M., Oskin, M., Burbank, D., and Alsdorf,, 2007. The Shuttle Radar Topography mission. Reviews of Geophysics, 45:33.

Government of Canada, Natural Resources Canada, 2000. Canadian Digital Elevation Data. Earth Sciences Sector, Centre of Topographic Information.

Jensen, J. R., 2007. Remote Sensing of the Environment, An Earth Resource Perspective. 2nd Edition. Published by Prentice Hall series in geographic information science.579.

Halls, H.C., 2009. A 100 km-long paleomagnetic traverse radial to the Sudbury Structure, Canada and it's bearing on Proterozoic deformation and metamorphism of the surrounding basement. Tectonophysics, 474: 493-506.

Hirano, A., Welch, R., and Lang, H., 2003. Mapping from ASTER stereo image data: DEM validation and accuracy assessment. ISPRS Journal of Photogrammetry & Remote Sensing, 57: 256-370.

Hirt C., Filmer M.S., and Featherstone, W.E., 2010. Comparison and validation of the recent freely available ASTER-GDEM ver1, SRTM ver4.1 and GEODATA DEM-9S ver3 digital elevation models over Australia, Australian Journal of Earth Sciences, 57(3): 337-347.

Jensen, J. R., 2007. Remote Sensing of the Environment, An Earth Resource Perspective. Pearson Education Inc., pp.592.

Krogh, T. E., Davis, D.W., and Corfu, F., 1984. Precise U-Pb zircon and baddeleyite afes for the Sudbury area. In the geology and ore deposits of the Sudbury Structure. Edited by Pye, E.G., Naldrett, A., Giblin, P.E. Ontario Geological Survey, Special Publication 1: 431- 446.

Lightfoot, P.C., and Keays, R.R., Morrison, G.G., Bite, A., Farrell, K., 1997. Geochemical relationships in the Sudbury Igneous Complex: Origin of the main mass and offset dikes. Economic Geology, 92: 289-307.

Lillesand, T.M, and Kiefer, R. W., 2000. Remote sensing of the Environment. Pearson Education Inc. 462-463

Massonnet, D., and Feigl, K. L., 1995. Discrimination of geophysical phenomena in satellite radar interferograms. Geophysical Research Letters, 22:1537 – 1540.Michalak J., 2004. DEM data obtained from the Shuttle Radar Topography Mission – SRTM-3. Annals of Geomatics, 2(1): 34–44.

Mitchell, G., 2011. Photosat. http://www.photosat.ca/. Date Accessed February, 2011.

Pike, R. J., 2002. A Bibliography of Terrain Modeling (Geomorphometry), the Quantitative Representation of Topography – Supplement 4.0. U.S. Geological Survey Open File Report 02-465, pp.157.

Slater, J. A., Heady, B., Kroenung, G., Curtis, W., Haase, J., Hoegemann, D., Shockley, C., and Tracy, K., 2001. Global Assessment of the new ASTER Global Digital Elevation Model. Photogrammetric Engineering & Remote Sensing, 77(4): 335-349.

Toutin, T., 2002. Three-Dimensional Topographic Mapping with ASTER Stereo Data in Rugged Topography. IEEE Transactions on Geosciences and Remote Sensing, 40(10): 2241-2247.

Toutin, T., 2002. Impact of terrain slope and aspect on radargrammetric DEM accuracy. ISPRS Journal of Photogrammetry & Remote Sensing, 57: 228-240.

Welch, R., Jordan, T., Lang, H., Murakami, H., 1998. ASTER as a source for topographic data in the late 1990's. IEEE Transactions on Geoscience and Remote Sensing, 36(4): 1282-1289.

Table 2.1.

Grid statistics for original and difference grids. Maximum elevation, minimum elevation, mean elevation, standard deviation.

	Maximum	Minimum	Mean	Std. Dev.
ASTER	596.6	105.4	413.1	44.5
SRTM	544.8	253.8	419.1	41.4
CDED	593.2	250.2	422.0	44.7
ASTER-CDED	138.3	-279.1	-5.0	10.2
ASTER- SRTM	139.0	-278.6	-5.0	17.4
CDED-SRTM	134.8	-121.0	-0.1	15.2

Table 2.2

Profile statistics for ASTER-CDED, ASTER-SRTM, and CDED-SRTM difference grids. Profiles1-8 run WNW, perpendicular to ASTER swath path. Profiles1a-4a run NNE. N = number of sample points, Maximum elevation, minimum elevation, mean elevation, standard deviation, Root mean square error, R^2.

Profiles	*N*	*Max*	*Min*	*Mean*	*S D*	R^2	*RMSE*
ASTER – CDED							
1	624	27.5	-44.3	-1.7	9.3	0.7	9.5
2	1048	35.8	-31.3	-3.8	10.6	0.9	11.2
3	1212	34.7	-42.3	-5.9	10.6	0.8	12.2
4	1340	39.1	-40.5	-5.3	9.7	0.8	11.0
5	1470	26.7	-56.0	-5.6	9.9	0.9	11.4
6	1531	27.9	-74.8	-6.1	9.8	1.0	11.6
7	1578	21.8	-55.4	-5.8	8.8	1.0	10.6
8	1341	28.5	-51.8	-5.8	10.0	1.0	11.5
1a	1259	43.0	-21.9	8.2	8.4	0.9	11.7
2a	1272	28.2	-47.8	-4.8	8.6	0.9	9.9
3a	1285	16.5	-72.9	-11.2	9.5	0.9	14.6
4a	1299	14.6	-32.7	-8.2	6.9	1.0	10.7
ASTER- SRTM							
1	873	51.2	-51.4	-3.34	13.4	0.4	12.9
2	1037	78.1	-51.0	-3.8	16.9	0.8	17.3
3	1205	43.0	-63.0	-7.2	17.8	0.5	16.4
4	1335	56.5	-56.1	-3.6	15.8	0.6	13.2
5	1456	50.7	-72.8	-4.6	17.9	0.7	18.5
6	1518	52.8	-106.4	-7.2	17.0	0.9	18.5
7	1567	67.2	-66.1	-4.8	14.5	0.9	18.1
8	1334	59.4	-81.2	-7.0	19.1	0.9	20.3
1a	1258	78.0	-42.0	8.0	16.4	0.8	18.3
2a	1268	43.9	-81.3	-5	16.9	0.7	17.6
3a	1280	37.9	-82.2	-10.8	18.1	0.7	21.1
4a	1304	87.8	-55.9	-9.3	16.4	0.8	18.8
CDED- SRTM							
1	622	53.8	-32.4	0.2	10.5	0.6	10.5
2	1037	82.4	-45.1	0.0	13.7	0.8	13.7
3	1205	31.7	-46.7	-1.4	9.05	0.7	9.1
4	1335	50.1	-39.7	1.7	12.1	0.6	12.2
5	1456	63.7	-47.0	1.0	14.7	0.8	14.7
6	1518	59.2	-47.1	-1.1	15.7	0.9	15.7
7	1567	68.4	-38.0	0.9	16.1	0.9	16.1
8	1334	65.2	-59.6	-1.2	17.0	0.9	17.1
1a	1257	65.1	-46.8	-0.1	15.4	0.8	15.4
2a	1265	51.5	-62.7	-0.2	14.7	0.8	14.7
3a	1275	51.2	-39.2	0.4	14.9	0.8	14.9
4a	1299	92.5	-47.6	-1.1	15.4	0.8	15.5

Table 2.3

Comparison of slope angle and density of vegetation. Profiles extracted from Figure 2.5 & 2.6.

ASTER					
	Max	Min	Mean	S D	ASTER vs. CDED R^2
Shallow Slope Dense Vegetation	16.7	-20.4	1.9	6.0	0.64
	6.8	-23.2	-4.1	5.5	0.96
Shallow Slope Sparse Vegetation	23.5	-47.5	-10	9.6	0.12
	9.6	-43.6	-11.2	7.4	0.79
Steep Slope Dense vegetation	39.9	-13.4	3.5	8.0	0.98
	39.1	-25.3	6.5	10.8	0.90
Steep Slope Sparse vegetation	26.5	-71.5	-10.0	10.4	0.90
	17.4	-42.7	-12.2	8.6	0.94
CDED					
	Max	Min	Mean	S D	ASTER vs. SRTM R^2
Shallow Slope Dense Vegetation	20.6	-19.1	5.1	8.1	0.42
	19.1	-32.8	-2.1	11.1	0.88
Shallow Slope Sparse Vegetation	22.6	-50.8	-10.2	9.31	0.16
	34.4	-59.0	-12.6	12.9	0.37
Steep Slope Dense vegetation	74.1	-80.7	2.2	30.5	0.77
	91.9	-38.0	8.1	22.8	0.70
Steep Slope Sparse vegetation	31.6	-91.6	-9.5	19.5	0.66
	36.0	-58.7	-13.0	16.9	0.73
SRTM					
	Max	Min	Mean	S D	CDED vs. SRTM R^2
Shallow Slope Dense Vegetation	17.8	-11.4	3.2	7.1	0.26
	21.5	-22.6	2	9.1	0.88
Shallow Slope Sparse Vegetation	9.7	-10.73	-0.2	3.9	0.50
	28.4	-19.9	-1.5	9.8	0.51
Steep Slope Dense vegetation	71.2	-80.1	-1.3	30.9	0.77
	69.1	-22.2	1.6	19.4	0.69
Steep Slope Sparse vegetation	33.9	-41.4	0.5	16.2	0.70
	49.9	-41.0	-0.8	16.7	0.76

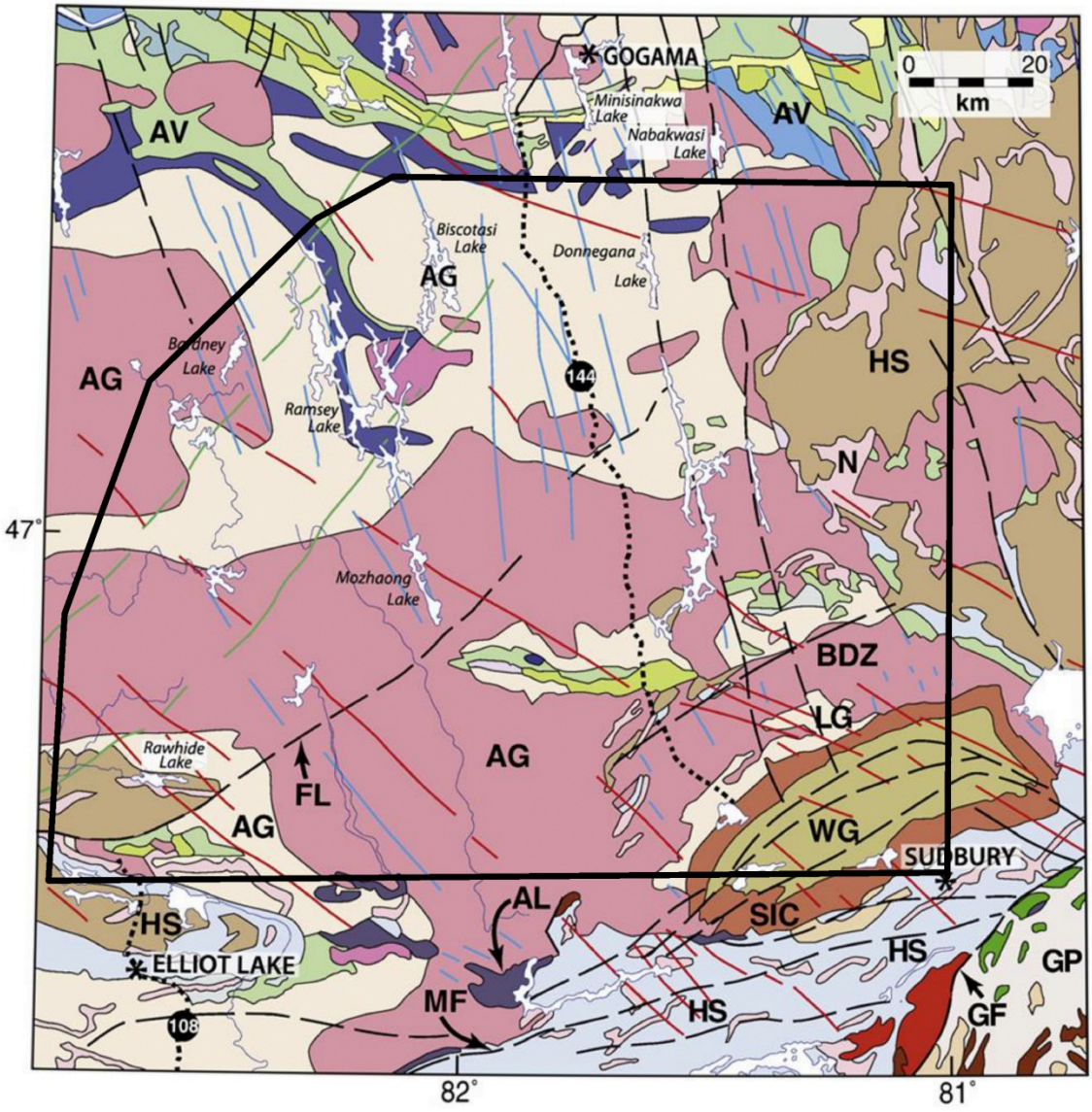

Figure 2.1.

Geological map of the study region, simplified from Geological Map 2543 of the Ontario Geological Survey (1991) From Halls 2009. "Sudbury Igneous Complex (SIC) and Whitewater Group (WG). Archean granite and gneiss (AG), Archean greenstone (AV), Levack Gneiss (LG), Agnico Lake intrusion (AL), Huronian Supergroup (HS), Nipissing diabase (N), Grenville Province (GP), Murray fault (MF),Grenville Front (GF), Benny Deformation Zone (BDZ) and Flack Lake fault (FL). The nature of Geological units not specifically labeled can be found in the legend of Map 2543 [visit http://www.geologyontario.mndm.gov.on.ca/]. The dykes of three swarms, the 2450 Ma Matachewan, 2170 Ma Biscotasing and 1230 Ma Sudbury, are shown respectively as blue green and red lines. Faults are shown as black dashed line" (Halls, 2009).

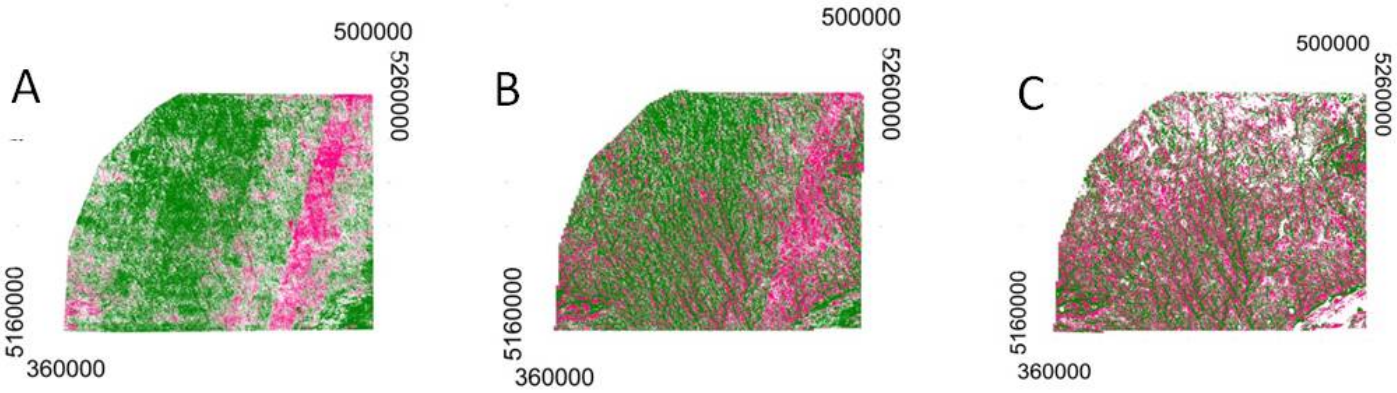

Figure 2.2

< 0

> 0

= 0

.

Difference grids. A=ASTER- CDED, B=ASTER-SRTM, C= CDED-SRTM.

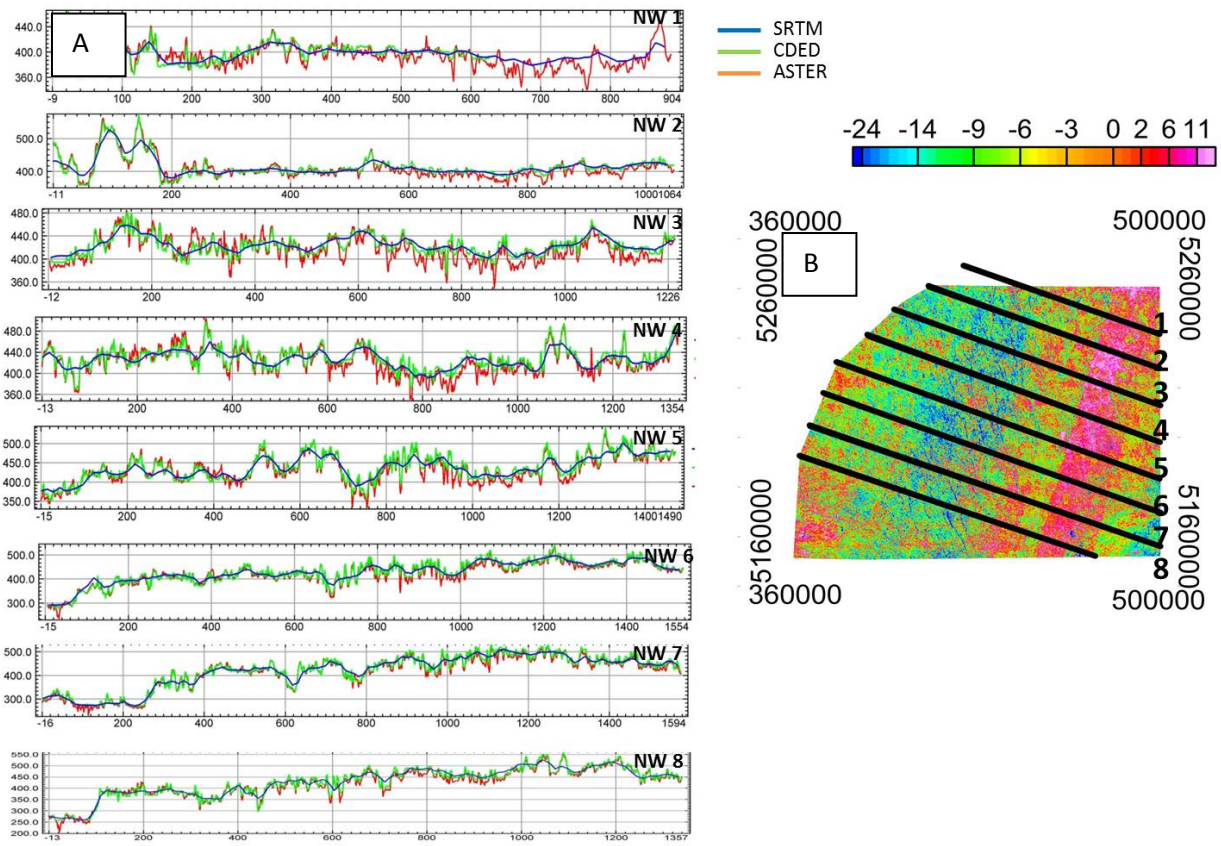

Figure 2.3.

(A) These profiles, labeled NW 1-8 correspond to the statistic in Table 2. (B) The ASTER-CDED grid is displayed to best portray the profile orientation with respect to the ASTER flight path. The pink rectangular feature corresponds to an error ASTER data along the flight path. The profiles are oriented perpendicular to the ASTER flight path.

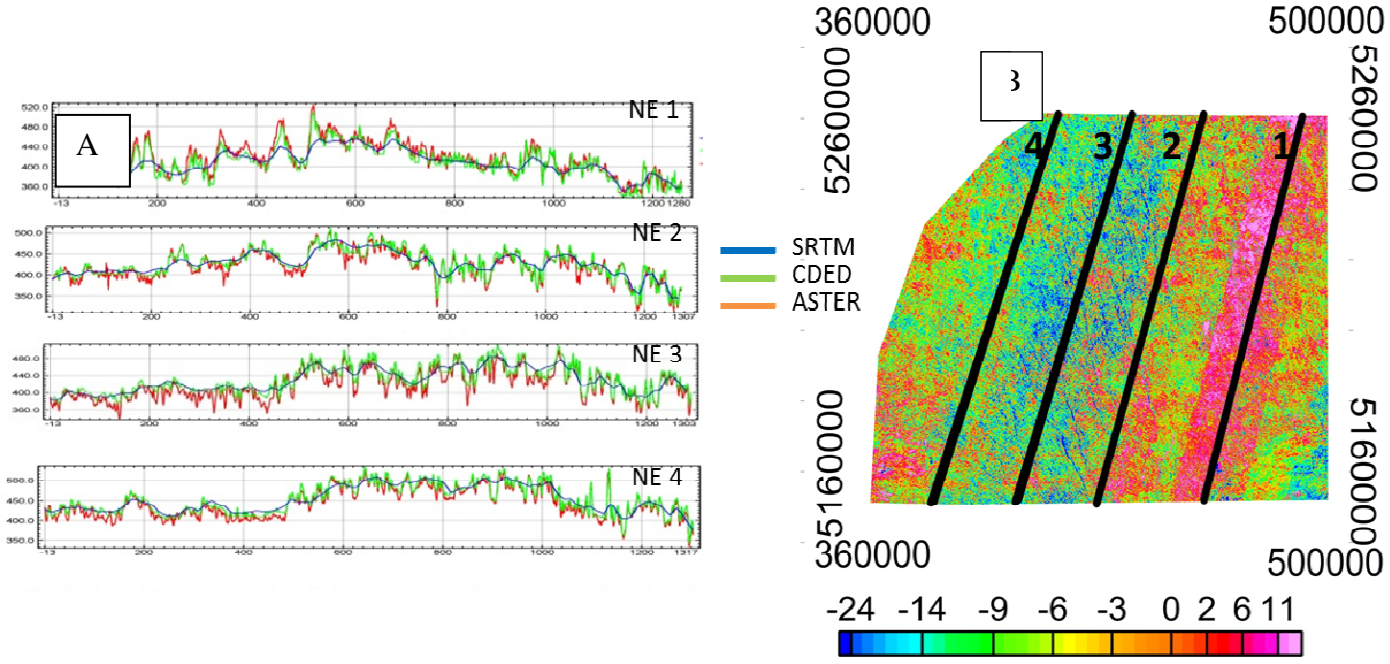

e ASTER-CDED
R flight path. The
ight path. The

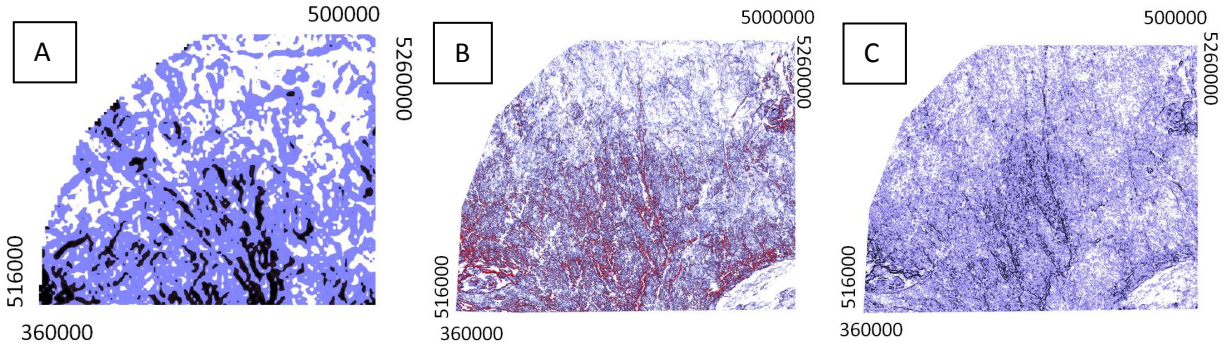

Figure 2.5

Slope grids of a) ASTER, b) CDED, c) SRTM. White = flat, blue = moderate slope, black = steep slope, red = very steep slope.

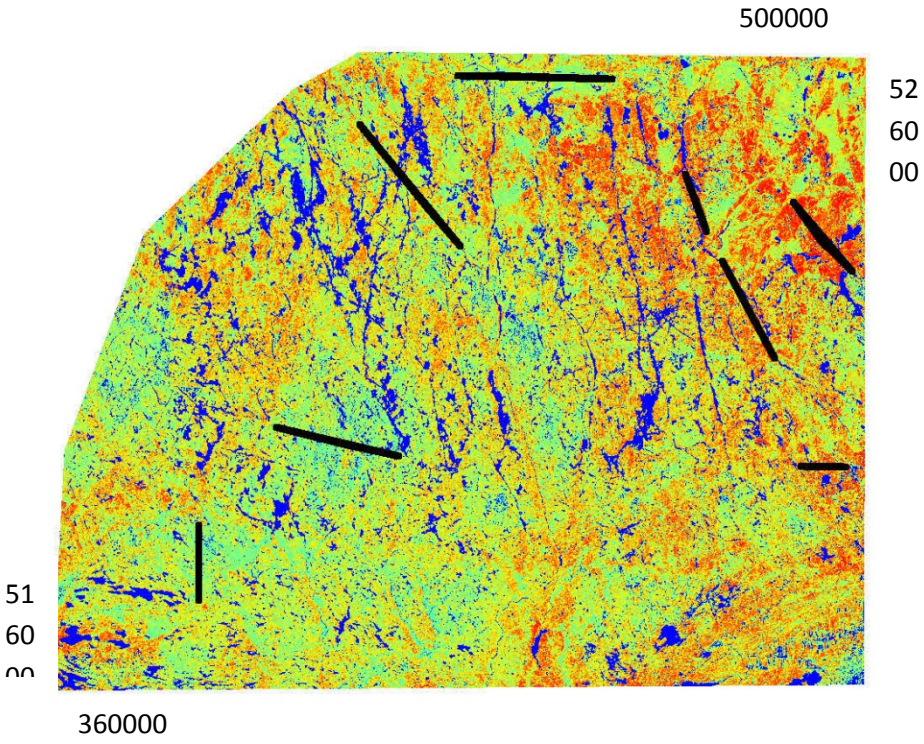

Figure 2.6

Normalized Difference Vegetation Index (NDVI) which shows the vegetation cover of the study area. It is calculated from Landsat TM images.

$$NDVI = \frac{\text{Band 4} - \text{Band3}}{Band\ 4\ +\ Band\ 3}$$

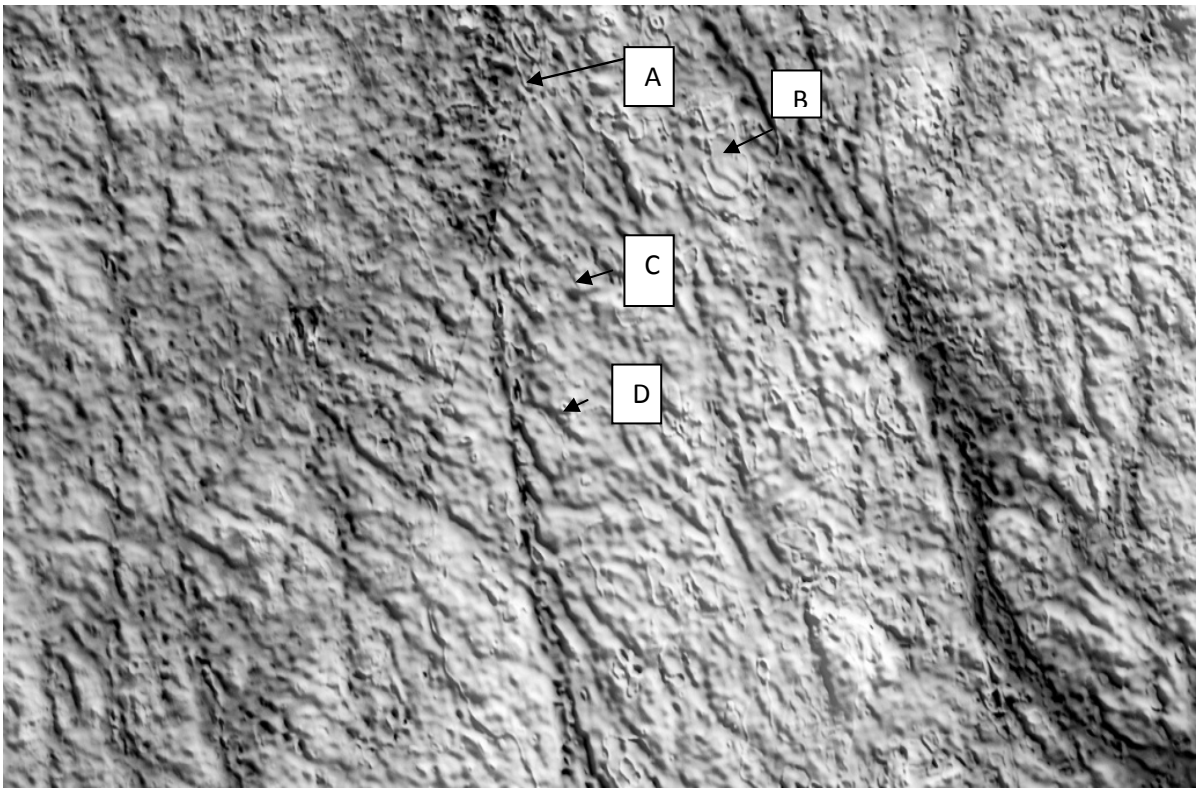

Figure 2.7
Shaded relief gray-scale grid of ASTER data from this study displaying four types of errors in ASTER data. The step anomaly in 'A' corresponds exactly with the western limit of the swath error. (A) Step anomaly from boundary between swath oriented stack numbers (ASTER validation paper, 2009), (B) Mole Runs, (D) Bumps, and (E) Pits

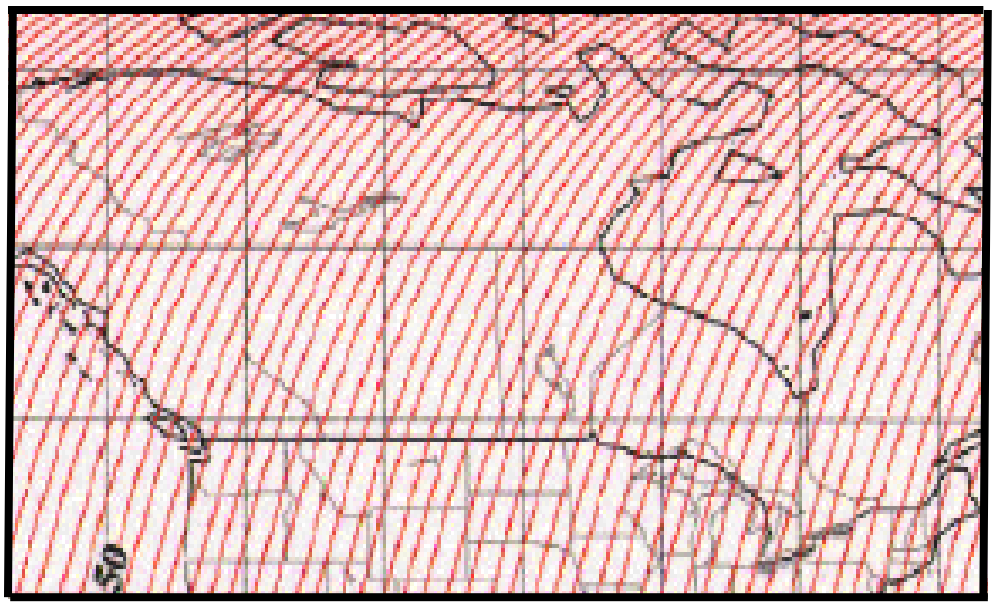

Figure 2.8
Approximate ASTER swath path Canada. Day time pass.

.

Chapter 3

Lineament Analysis of the Superior Province, Canada;

Evidence for a multi-ring basin?

Introduction

In this study we analyze the fracture density pattern as revealed by digital topography for an area 140km by 110km in north central Ontario (Figure 3.1).The most dominant lithological and structural feature present in this area is the 1.85 Ga Sudbury Structure (SS) (Dressler, 1991). Lithological evidence in support of a meteorite origin for the SS includes the Sudbury Igneous Complex (SIC) that represents the original melt sheet and the thermally modified fall back breccia of the Onaping Formation (Ames et al., 2005). Additional features associated with the impact event include shatter cones, pseudotachylites, and injected breccia all of which exhibit a systematic spatial distribution relative to the basal contact of the SIC (Riller, 2005).

Geologically the terrain is heterogeneous. The SS lies on the transition between Archean aged greenstones, granites, and gneisses of the Superior Province and the unconformably overlain Huronian sediments of the Southern Province (Lafrance et al., 2008; Rousell et al., 1998, Halls, 2009). This area has experienced a number of temporally distinct geological events; for example there have been at least three orogenic events that could have caused faulting in the Superior Province. The Blezardian Orogeny is thought to have occurred 2.4- 2.2 Ga, the Penokean Orogeny, 1.89-1.83 Ga, and the Grenville Orogeny, 1.12-0.98 Ga (Riller, 1999; Carr, 2000). Each of these events has had the potential for producing distinctive patterns in the current topographic record. Dike swarms are characterized by swaths of sub-parallel lineaments. Three swarms of dikes have been mapped within the study area; 2.47 Ga Matachewan dykes, ~2.2 Ga Nippissing sills, and 1.24 Ga Sudbury dykes (Siddorn, 2002). Other dike swarms are certainly present but they have not been formally named (Siddorn, 2002). Besides these, there are numerous fracture patterns in the study area that cannot be definitively associated with any of the known orogenic events (Riller, 2005). Analysis of their patterns will help determine if they are instead associated with the Sudbury impact crater. There is still no consensus as to the original morphology of the crater.

Four types of impact crater morphologies have been observed in our solar system; simple, central peak, peak ring and multi ring (Turtle, 2005). At the smaller end of the spectrum are simple craters aptly named for their structure-less interior; with a diameter generally less than 3-5 km (Turtle, 2005). At the 3-5 km threshold craters begin to display different types of modification and as such are termed complex craters. With larger crater sizes, the crater floor rebounds vertically during the early stages of crater formation (Turtle, 2005). This results in a relatively flat floor that isn't strongly correlated with crater diameter. In the smaller types of complex craters, central peaks are produced from the rebound of the floor which causes rocks in the center of the crater to be lifted above the floor, creating a large mound. Central peaks are built larger by the inward sliding of debris from the crater wall (breccia and melt). As the crater diameter continues to increase, the central peak transitions into a peak ring, where the uplifted material forms a discontinuous ring of mountains within the outer rim of the crater (Turtle, 2005). Finally the largest impact craters are known as multi-ring basins (Turtle, 2005). Characteristic of this type are the presence of ring shaped faults and fractures beyond the crater rim. There are two subtypes of multi-ring basins. One has several inward facing fault scarps while the second exhibits tens to hundreds of outward facing scarps (Turtle, 2005; Croft, 1981).

Recognition of the presence, or absence, of these rings therefore has direct implications for the original size of an impact crater. In 1994, Hayden Butler reported results of a traditional lineament analysis for a region to the north of the SIC. Butler (1994) chose to study this region since it has always been considered to contain the least deformed portion of the Sudbury crater. Butler's analysis was primarily based on the visual recognition of lineament features in Landsat imagery. If these lineaments are genuinely associated with genesis of the SIC then their distribution pattern should have some geometrical similarity to the SIC – Levack Gneiss contact if that contact represents the crater floor to wall transition. To test for this possibility Butler systematically eliminated lineaments that did not approximate this geometry. Following data processing, Butler (1994) suggested there was evidence for an increased density of lineaments

with similar geometry to the SIC-LGC contact at about 25 -30 km (a ring of 130km diameter) from north of the SIC contact, which closely corresponds to the measured 25 km anomaly in this study. He mathematically interpolated the location of four other crater rings (figure3.2) at 30, 90, 180, and 270 km diameters (which are observed ~15km south of the northern SIC contact, and ~15 , ~60, and ~100km north of the SIC) (Butler, 1994). Subsequently, the rings initially mapped by Butler (1994) have appeared in numerous publications (Spray 2004, Grieve et al., 2008). Interpretation of these rings has become central to discussions regarding the original size of the Sudbury Impact Crater. Estimates for the hypothesized original crater dimensions vary from 180 km (Spray, 2004; Butler, 1994) to 260 km (Turtle et al., 2005). In this hypothesis the four rings are at 90 km, central uplift; 130 km, transient crater; 180 and 260 km are estimated to be the final crater rim diameter (Butler, 1994; Spray, 2004). A number of more recent structural studies on different aspects of the Sudbury impact crater appear to be in conflict with the simple concentric ring pattern reported by Butler (1994). For example, it has been suggested that these ring-like structures map the outline of large scale fault structures (Spray 2004). Yet Grieve et al., (2008) noted that the presence of Huronian age sediments thought to be located between the 90 and 130 km rings is not possible if the 130 km ring did indeed represent the diameter of the transient crater, since everything within that ring would have been excavated. The Sudbury impact crater has been deformed from originally circular shape to elliptical with a long axis of approximately 62 and a short axis of approximately 27 km (Morris, 2002). The most generally accepted explanation for this extreme deformation is a Penokean age folding event during which the South Range was emplaced over the North Range (Shanks and Schwerdtner, 1991; Riller 2005). This proposed folding event however, may be at odds with the distribution of impact related rings mapped by Butler (1994). The North Range of the SIC is dipping at 35^{o}+ to the south-south-east so at some point this dip must become horizontal. Folding would produce a progressive change in dip with increasing distance from the fold axis. Such a change in dip versus distance must produce a distortion in the ring pattern. If the rings do follow the North

Range contact as suggested by Butler (1994) then this must mean that this area cannot have been folded.

At the time that Butler (1994) reported his initial study it was common practice to extract lineament information from spectral images, such as Landsat TM. Most of these studies are pseudo-quantitative since they rely on the skill of the interpreter to visually analyze the data. When using spectral images several features can represent geologic structures. Abrupt changes in vegetation or soil type can be indicative of a change in host rock composition and rivers often indicate the location of a fault or fracture (Papadaki et al., 2011). Using various spectral bands, these and other representative features can give a good estimation of the faulting and fracture pattern present in a given region. In the nearly twenty years since Butler's original work there have been two major technological advances which directly affect this study.

First, with the increased availability of digital high resolution (<100 m) topographic datasets it is now possible to extract lineament information directly. Central to this analysis is the logical association of topographic lows with faults or fractures; it is assumed that topographic lows arise as a result of locally increased weathering promoted by increased rock brecciation (Koike et al., 1995; Papadaki et al., 2011). Digital topography covering the study area is available from three different sources: 1) aerial photography derived from the Canadian Digital Elevation Database (CDED) of digital topography; 2) Space Shuttle derived radar imaging from the Shuttle Radar Topography Mission (SRTM); and 3) TERRA satellite imagery based on the Advanced Space borne Thermal Emissions and Reflection Radiometer (ASTER) DEM. In a companion study (this thesis Chapter 1) we have shown that there are only minor data differences between the various datasets. None of the differences would impact on the lineament analysis. For this study we used the ASTER dataset since it offered better spatial resolution that the SRTM data and more reliable elevations than CDED. The second technological advance over this same time period is that methods for quantitative analysis of spatially dependent variables, known as Geographic Information Systems (GIS) have become readily available. There are a

number of software packages that can quantitatively examine the distribution of topographic features relative to known geometry.

This study re-examines Butler's original suggestion that there are a series of impact related ring-like structures surrounding the North Range of the Sudbury Impact Structure, especially on evidence for the existence and locus of the 130km of Butler's rings. Results are derived from a quantitative investigation of the spatial distribution of valleys and depressions present in the digital topographic record. The data strongly supports Butler (1994) interpretation of a down faulted block associated with a local ring structure. This reinforces the idea that the Sudbury Impact Crater is a multi-ring structure with a ring about 130km in diameter and 25 km north of the SIC basal contact.

Data Acquisition

The topographic data used in this study was downloaded from the ASTER website (http://asterweb.jpl.nasa.gov/). ASTER is one of five remote sensing systems aboard the Terra Satellite launched in 1999. Elevation is calculated from two views of the surface acquired during one pass. While using the same wavelength one of the two views is vertical and the other is inclined. Simple trigonometry of matching common points in the two scenes provides an estimate of the elevation for each pixel point. Verification studies which compare ASTER elevations to other data sources such as CDED, or SRTM suggest that ASTER elevations are on average ~5 m lower than other DEMs (this thesis Chapter1, ASTER Validation, 2009). Other errors known to be present in ASTER DEM's data include: 1) 'step anomalies', usually found in regions of overlap between adjacent swath paths; and 2) bumps, pits that are randomly distributed positive and negative anomalies (respectively), and mole runs that are positive curvilinear anomalies that take the extended shape of some curvilinear stack number boundaries and occur primarily in flat terrain. Since ASTER DEM's are derived from imagery in the visible electromagnetic spectrum, cloud cover will inhibit data acquisition.

None of the errors associated with ASTER DEM's will have any direct effect on the results of this analysis. Since the focus of this study is the identification of localized elongate depressions, the absolute accuracy of the elevation surface is not essential. None of the known errors will produce laterally continuous elongate features that could be mistaken for topographic depressions. Of the three data sets available ASTER was chosen because it provided the most continuous coverage with the smallest pixel spacing.

Methodology

Topographic lows were determined in two ways: 1) tilt, and 2) stream flow analysis. Tilt is a method used in potential field geophysics to determine edges in the data. The surface of a potential field data set is wave like and has peaks and troughs representing geological features, very similar to how DEM data is gridded and visualized. Tilt uses first derivatives of the X, Y, and Z planes of the surface, be it part of the electromagnetic spectrum or a true representation of a surface to determine their rate of change. In the ASTER data, these edges represent rapid change in elevation. The total field (TF) input when using topographic data represents the entire original dataset. The horizontal gradient magnitude (HGM) refers to the extent of change in the X, Y plane. Tilt is emphasizing the distribution of localities with steep slope. The expression below was taken from Pilkington and Keating (2004).

Total Field (TF) - Horizontal Gradient Magnitude (HGM) = $\sqrt{\left|\left\{\frac{dT}{dx}\right\}^2 + \left\{\frac{dT}{dy}\right\}^2\right|}$

Tilt = $\tan^{-1}\left\{\frac{\frac{dT}{dz}}{TF-HGM}\right\}$

The stream flow analysis detects topographic lows by mimicking a hydrological catchment area by identifying the continuity of local depressions in the topographic surface. Computation of the stream flow network is achieved by the comparison of the elevation of an individual cell to that of the surrounding cells. Flow is mapped by connection to adjacent windows of data until a continuous network of flow is completed. Limitations of the method can

include bounds on elevation differences and the minimum dimension of a watershed. (MapInfo, 2007). When using data such as ASTER that is known to contain localized artifacts (pits) which will affect the stream flow computation it is necessary to manually override such problems. Stream flow then defines linearly continuous topographic lows.

Having first identified the spatial distribution of possible fractures the systematic relationship between the orientation of the fractures and the contact of the Sudbury Igneous Complex (the base of the impact melt sheet) was determined. There are number of possible approaches to this step. Butler (1994) employed a vector-based approach: he selectively eliminated all lineaments that did not have a similar orientation to the trend of the SIC contact. In this study we have adopted a raster-based approach. First, the outputs from the stream flow and tilt grids of ASTER were converted into point files, with each linear feature being transformed into a series of many points. Second, the spatial distribution of lineaments in relationship to the SIC were computed by using a series of buffers following the exact geometry of the northern SIC contact with 50 m increments up to a distance of 35 km north of the SIC - LGC contact. After each buffer increment the number of points located between the outer buffer boundary and the SIC contact was counted. By subtracting sequential buffer increments it is possible to count the number of responses in each 50 m buffer window. The rationale behind this approach is that whenever a lineament feature corresponds perfectly to the geometry of the SIC contact, it would output a maximum number of points in that particular buffer. Linear features at an angle to this contact would crosscut several buffers, therefore outputting only a fraction of its points into any given buffer. The output data was then graphed as distance from the SIC northern contact against frequency of points. To reduce the noise, a moving average filter of 5 was applied to the data. Systematically incrementing the buffer by 50 m from 0 to 35 km means that there will be a corresponding systematic increase in the area incorporated in each buffer segment. This in turn would produce an increase in number of points. This problem was easily overcome by removing a linear slope from the results.

The buffering approach outlined above serves to accentuate larger scale features, specifically a more continuous ring like structure. It is incapable of mapping situations where there are a series of short sub-parallel features. Also this regional-style counting method provides no information regarding the sense of motion on the fault surfaces. If the lineaments are genuinely fault slopes related to the collapse of an impact crater then all of the faults should be showing the same sense of imbrications. This issue can be addressed by analyzing the spatial distribution of surface aspect associated with the fracture points. The aspect map shows the down slope direction while also showing its steepness (Papadaki, 2011). Computing a kernel density distribution determines the density of points near any raster cell (Silverman, 1986). The kernel estimator, Gaussian probability estimation, was set at 5 km and the window width, which smooth's the data was set at 200m.

To demonstrate the validity of these approaches a synthetic model was created to roughly represent the fault and fracture pattern in the study area (Figure 3.3). This model had lineaments with various azimuths, some parallel to the 'synthetic SIC' contact, others directly orthogonal, and several in between. This model was processed the same as the ASTER data, with stream flow excluded. A buffer was carried out at three intervals 50 m, 100 m and 200 m.

Results and Discussion

Synthetic model

The synthetic model in figure 3.4 clearly shows the presence of two linear features located within 200 m of the actual feature. As was expected, the 50 m buffer was the most accurate, followed by the 100 m and then 200 m buffers. The extreme difference in number of points demonstrates how features that mimic the exact geometry of the buffer create a significant peak in resulting data. The features not mimicking the buffer geometry were still counted and appear as small bumps in the data, significantly out-weighted by the larger peaks.

Superior Province

The 1000 m resolution data is extremely noisy, as can be seen by the number of peaks and troughs in Figure 3.5. The actual number of point (frequency of points) is irrelevant; it is the relative difference that shows the areas of interest. There are three key areas of greater number of points; 25 km, 52-60 km and 73 km. Butler's (1994) 3rd ring lies at 130km diameter, corresponding with this study's 25km anomaly, his 4th ring lies at ~58 km, corresponding very well with the 52 to 60 km anomaly in this study and his 5th ring lies at ~95 km north of the SIC which does not correspond to any anomalies in this study's data. These peaks were chosen visually instead of statistically due to the lack of a tested method and statistically significant threshold. The 3rd ring was chosen for a more detailed study due to its proximity to the Sudbury impact crater and the similarity in location to Butler's (1994) 3rd ring, which was his most well observed. A detailed examination of the area between 1 – 34 km north of the SIC at 50 m buffer increments (figure 3.6 and 3.7). This higher resolution analysis not only agrees with the 1000 m analysis that there is something of interest at ~25 km, but has also revealed the presence of anomalies at ~ 3km, ~13km and ~18 km north of the SIC contact. These anomalies are not clear single peaks as in the synthetic model, making interpretation significantly more difficult. The 90 km ring (15 km north of SIC) corresponds to the 13km anomaly north of the SIC.

The width of the observed anomalies suggests that the down faulted ring grabens, noticed by Butler (1994) and Spray (2002) are not single slip surfaces but rather are highly fractured areas. Each anomaly is defined by an increase in fracture density, sometimes up to several kilometers from peak, followed by a similar decrease. Since several of the anomalies do correspond to Butler's (1994) rings, it suggests the authenticity of the anomalous results of this study. It also begs the question of what the other anomalous features represent. The kernel density analysis of the stream flow data displays an obvious continuity at 25km north of the SIC, indicating a ring structure parallel to the geometry of the SIC northern contact (figure 3.8 & 3.9). The aspect map clearly shows the density of slopes identical to that of the SIC (figure 3.10). These pieces of evidence combined may indicate that the Sudbury crater is a multi-ring basin

with many ring features, and perhaps one or two large faulting events, instead of the previously held view of simply 5 large slip surfaces.

Conclusion

Using a topographically based approach to lineament analysis, this study has verified the presence of rings associated with the 1.84 Ga Sudbury Impact Crater. The presence of these rings implies that the crater is a multi-ring basin. Several of the anomalies in this study correspond very closely with rings 2, 3 and 4 (Butler, 1994). The most prominent anomaly is located 25 km north of the SIC basal contact and corresponds closely to the highly defined 3rd ring of Butler (1994). This suggests that perhaps the multi-ring basin had several down faulted blocks representing ring structures. Further analysis should be completed on the area north of Butler's (1994) 3rd ring to determine the full extent of the crater.

References

Ames, D.E., Buckle, J., Davidson, A., and Card, K., 2005. Sudbury bedrock compilation; Geology: Geological Survey of Canada, Open File 4570, scale 1:50 000.

ASTER GDEM Validation Team: METI/ERSDAC, NASA/LPDAAC, USGS/EROS, 2009. ASTER Global DEM Validation Summary Report, http://www.ersdac.or.jp/GDEM/E/image/ASTERGDEM_ValidationSummaryReport_Ver1.pdf, last access April 2011

Butler, H. R., 1994. Lineament analysis of the Sudbury multiring impact Structure. Geological Society of America, Special Paper 293.

Carr, S.D., Easton, R.M., Jamieson, R.A., Culshaw, N.G., 2000. Geologic transect across the Grenville Orogeny of Ontario and New York. Canadian Journal of Earth Sciences, 37: 193-216.

Croft, K.S., 1981. The modification stage of basin formation: Conditions of ring formation. Multi-ring Basins, Proc. Lunar Planet. Sci., 12A: 227-257.

Dressler, B.O., Gupta, V.K. and Muir, T.L., 1991. Chapter 15: The Sudbury Structure. In: Thurston, P.C., Williams, H.R., Sutcliffe, R.H. and Stott, G.M., Editors, 1991. *Geology of Ontario*, Ontario Geological Survey, Toronto, Special Volume, 593–625.

Grieve, R.A.F., Reimold, W.U., Morgan, J., Riller, U., Pilkington, M., 2008. Observations and interpretations at Vredefort, Sudbury, and Chicxulub: Towards an empirical model of terrestrial impact basin formation. Meteoritics & Planetary Science, 43(5): 855-882.

Halls, H.C., 2009. A 100 km-long paleomagnetic traverse radial to the Sudbury Structure, Canada and it's bearing on Proterozoic deformation and metamorphism of the surrounding basement. Tectonophysics, 474: 493-506.

Koike, K., Nagano, S., Ohmi, M., 1995. Lineament analysis of satellite images using a segment tracing algorithm (STA). Computers & Geosciences, 21(9): 1091-1104

Lafrance, B., Legault, D., Ames, D.E., 2008. The formation of the Sudbury breccia in the North Range of the Sudbury impact structure. Precambrian Research, 165: 107-119.

MapInfo., 2007. Map Info Professional, version 9.0 user guide. Pitney Bowes MapInfo Corporation, pp.568.

Morris, W.A., 2002. The Sudbury Structure: A circular impact crater? Geophysical Research Letters, 29(20): 63-1 – 63-4.

Papadaki, E. S., Mertikas, S.P., Sarris, A., 2011. Identification of lineaments with possible structural origin using ASTER images and DEM derived products in Western Crete, Greece. EarSeL e Proceedings, 10: 9-26.

Pilkington, M., and Keating, P., 2004. Contact mapping from gridded magnetic data- a comparison of techniques. Exploration Geophysics, 35: 306-311.

Riller, U., 2005. Structural characteristics of the Sudbury impact structure, Canada: Impact-induced versus orogenic deformation- a review. Meteoritics & Planetary Science, 40(11): 1723-1740.

Riller, U., Schwerdtner, W.M., Halls, G.C., Card, K.D., 1999. Transpressive tectonism in the eastern Penokean orogeny, Canada Consequences for Proterozoic crustal kinematics and continental fragmentation. Precambrian Research, 93: 51-70.

Rousell, D.H., and Long, D.G.F., 1998. Are Outliers of the Huronian Supergroup preserved in Structures Associated with the Collapse of the Sudbury Impact Crater? Journal of Geology, 106: 407-419.

Siddorn, J.P., Halls, H.C., 2002. Variation in plagioclase clouding intensity in Matachewan dykes: evidence for the exhumation history of the northern margin of the Sudbury Igneous Complex. Canadian Journal of Earth Science, 39: 933-942.

Silverman, B.W., 1986. Density estimation for statistics and data analysis. Monographs on Statistics and Applied Probability, London, Chapman Hall, pp. 22.

Shanks, W. S., and Schwerdtner, W. M., 1991. Crude quantitative estimates of the original northwest-southeast dimension of the Sudbury Structure, south-central Canadian Shield. Canadian Journal of Earth Science, 28: 1677-1686.

Spray, J. G., Butler, H. R., Thompson, M.L., 2004. Tectonic influences on the morphometry of the Sudbury impact structure: Implications for terrestrial cratering and modeling. Meteoritics and Planetary Science, 34(2): 287-301.

Turtle, E.P., Pierazzo, E., Collins, G.S., Osinski, G.R., Melosh, H.J., Morgan, J.V., Reimold, W.U., 2005. Impact Structures: What does crater diameter mean? Geological Society of America, Special Paper 384.

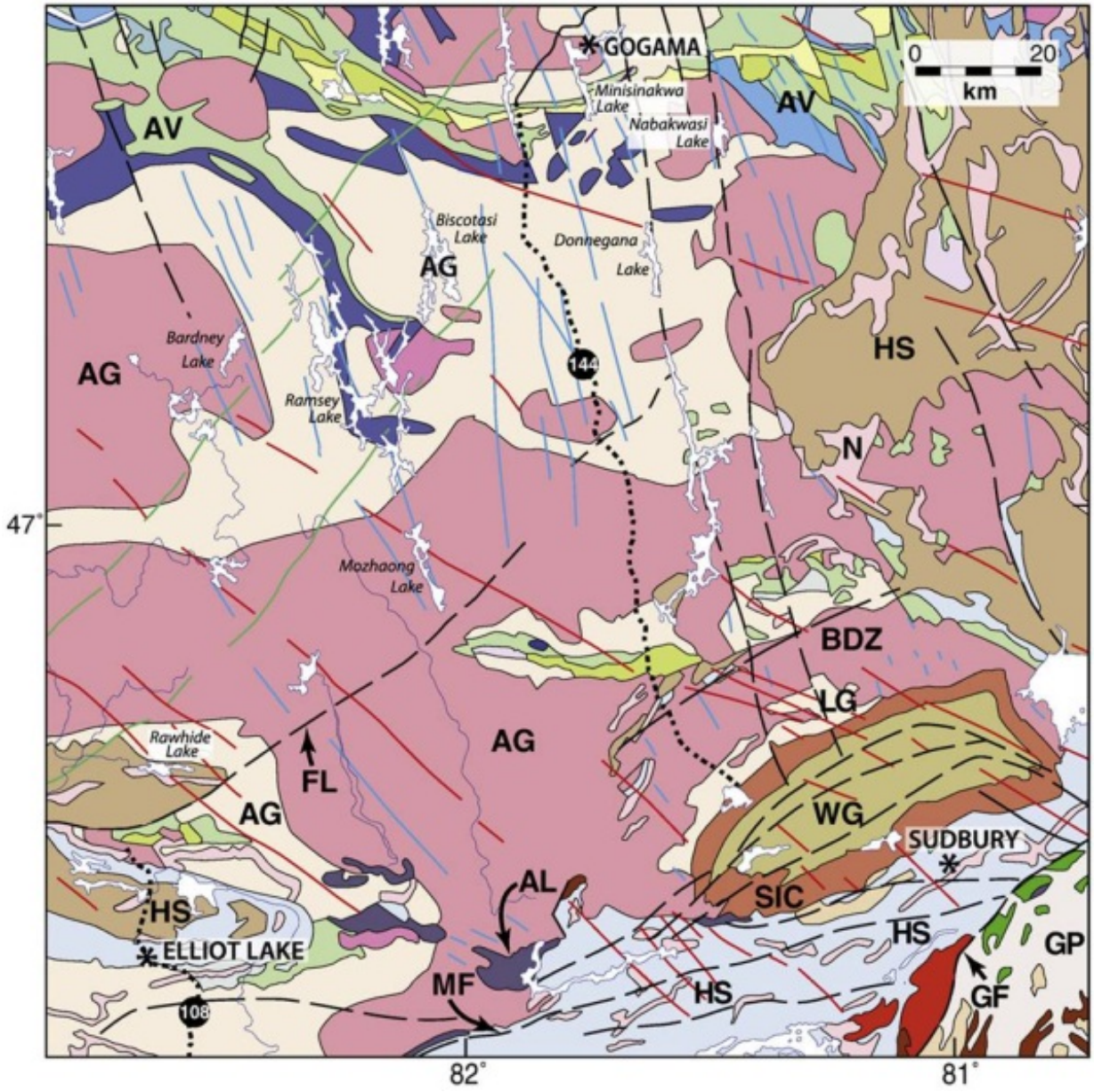

Figure 3.1

Geological map of the study region, simplified from Geological Map 2543 of the Ontario Geological Survey (1991) From Halls 2009. "Sudbury Igneous Complex (SIC) and Whitewater Group (WG). Archean granite and gneiss (AG), Archean greenstone (AV), Levack Gneiss (LG), Agnico Lake intrusion (AL), Huronian Supergroup (HS), Nipissing diabase (N), Grenville Province (GP), Murray fault (MF),Grenville Front (GF), Benny Deformation Zone (BDZ) and Flack Lake fault (FL). The nature of Geological units not specifically labeled can be found in the legend of Map 2543 [visit http://www.geologyontario.mndm.gov.on.ca/]. The dykes of three swarms, the 2450 Ma Matachewan, 2170 Ma Biscotasing and 1230 Ma Sudbury, are shown respectively as blue green and red lines. Faults are shown as black dashed line" (Halls, 2009).

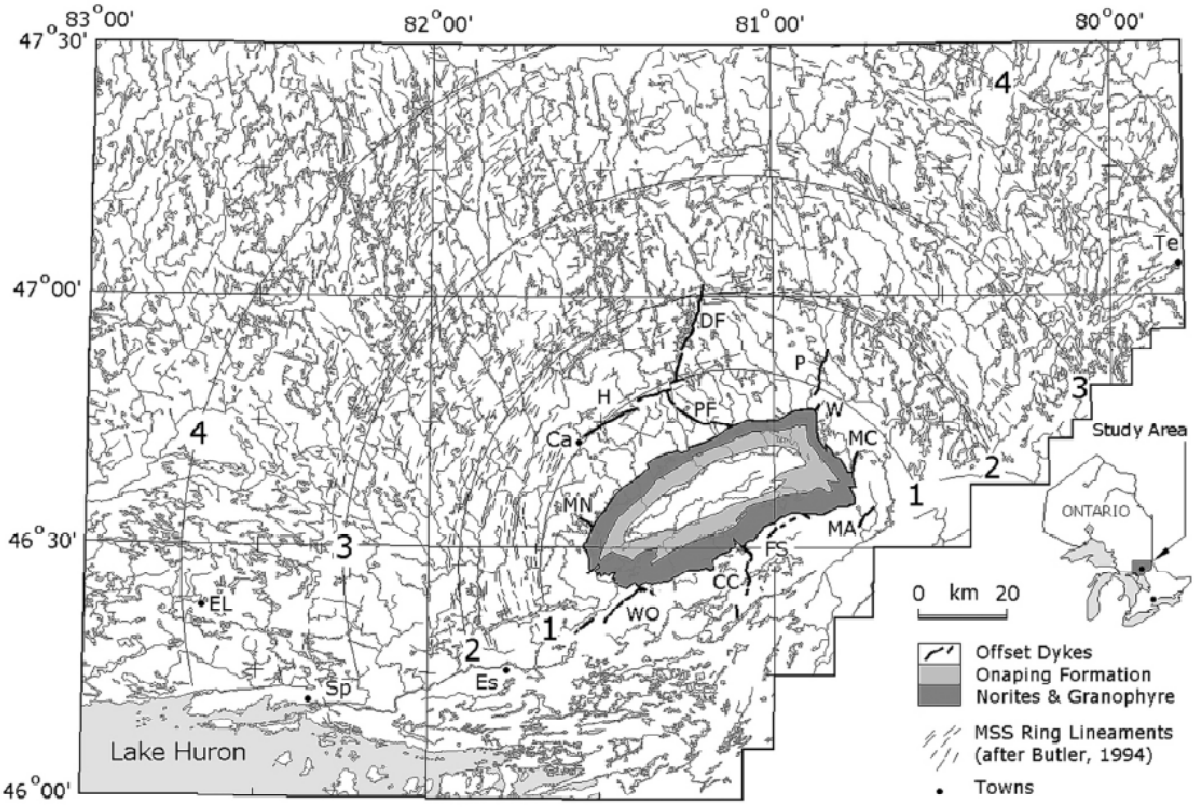

Figure 3.2

Concentric lineament features as calculated by Butler (1994; from Spray et al. 2004)

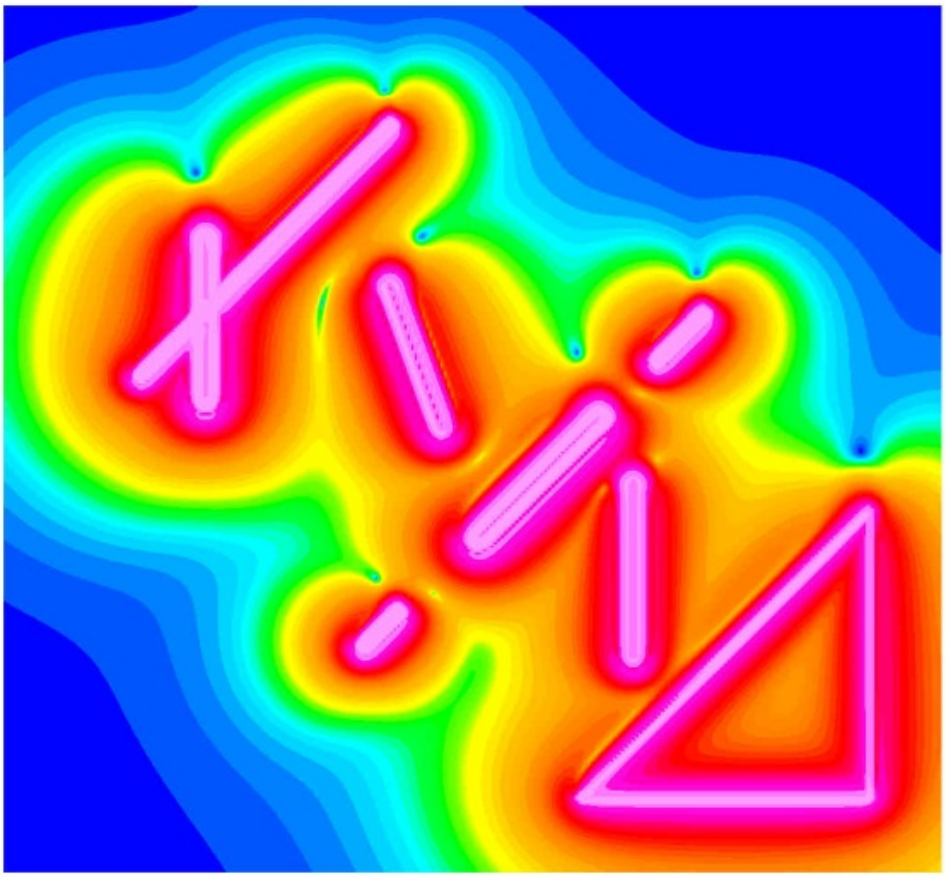

Figure 3.3

Synthetic model. Created in Encom ModelVision, this model mimics the geometrical relationship between the lineaments in the Superior Province, Ontario, and the northern SIC contact.

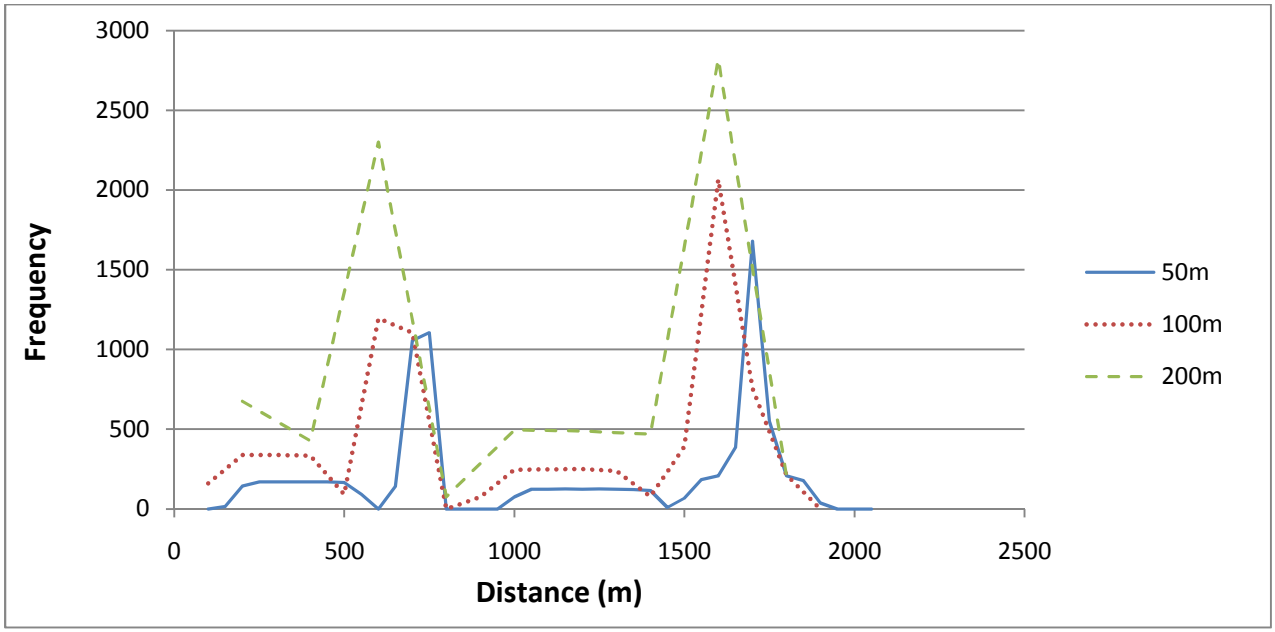

Figure 3.4

Buffer results of the synthetic model. Buffer interval was increased from 50m to 200m. This resulted in a migration of the anomalous peaks but they remain prominent in all analyses.

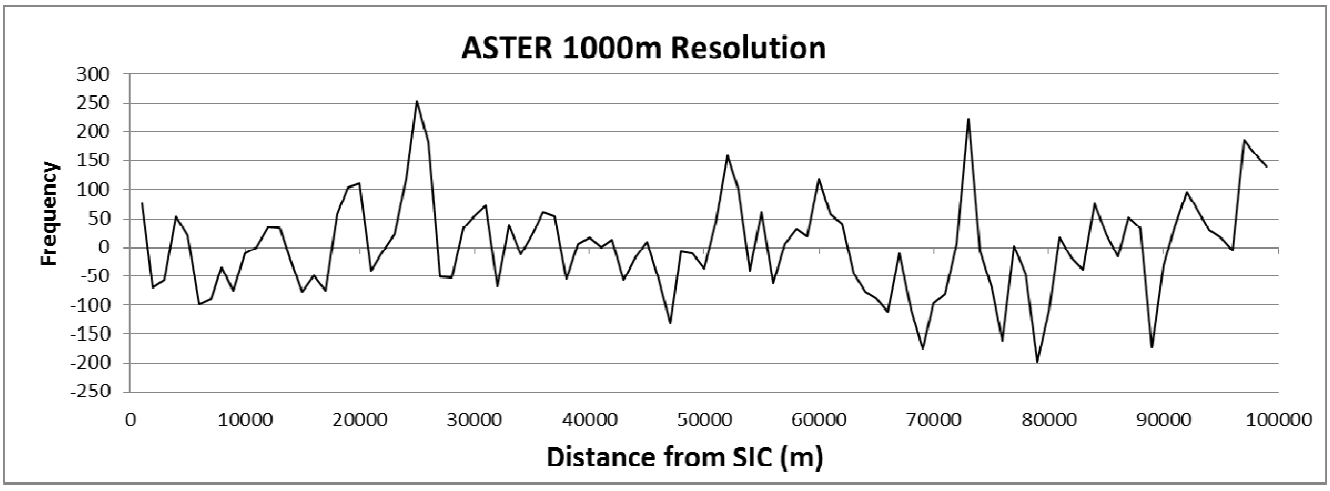

)0m increments.

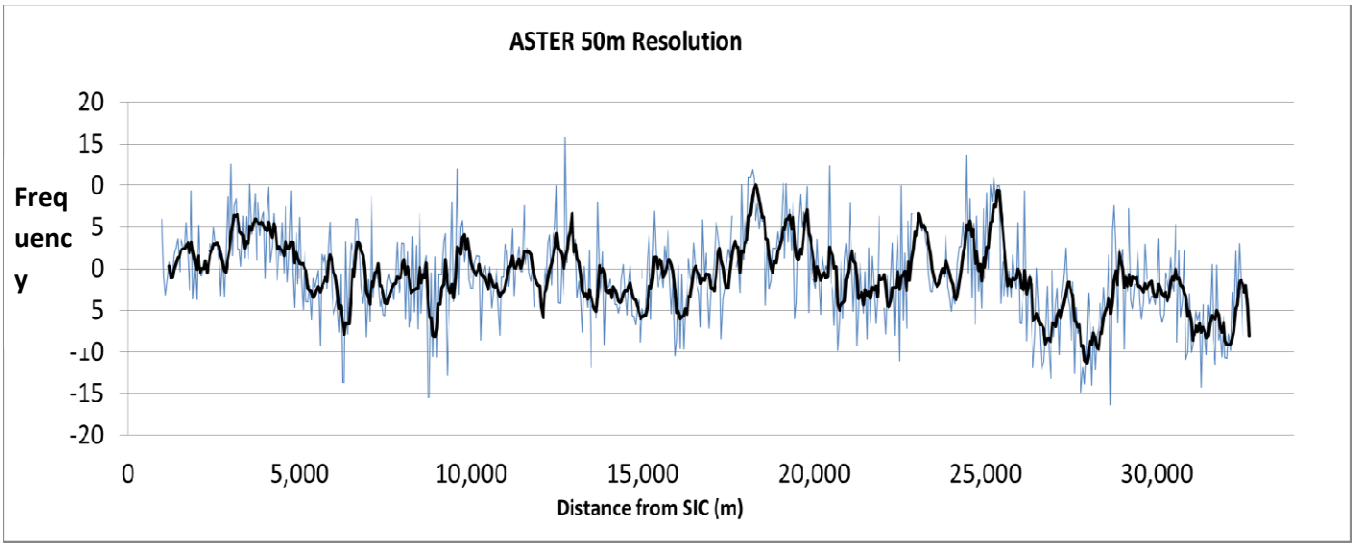
ASTER 50m Resolution
Frequency
20
15
0
5
0
5
-10
-15
-20
0
5,000
10,000
15,000
20,000
25,000
30,000
Distance from SIC (m)

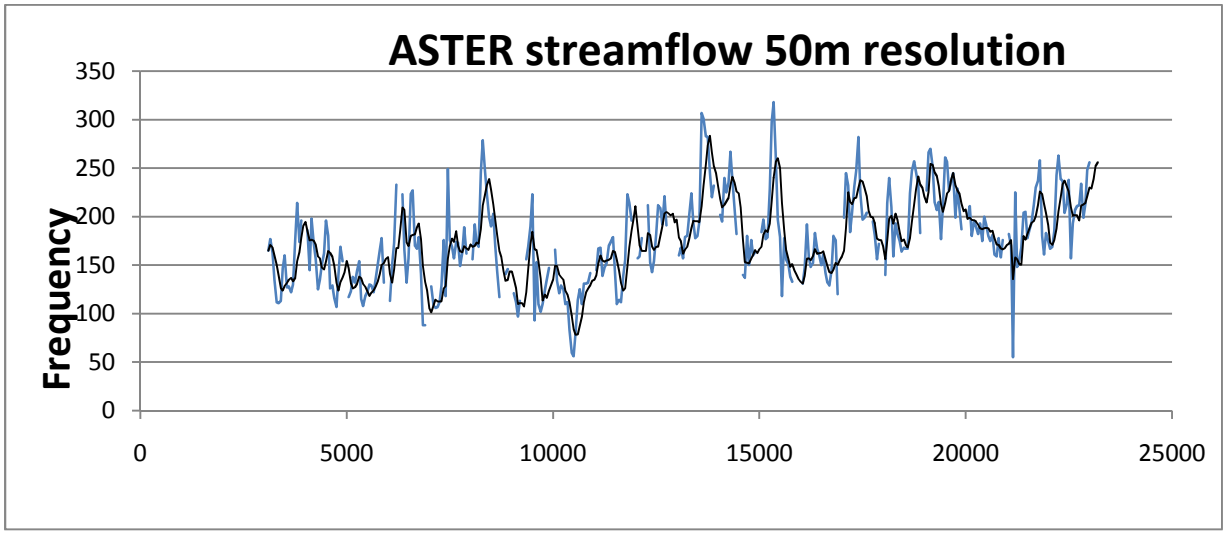

Figure 3.7

Buffer analysis of ASTER stream flow at 50m resolution

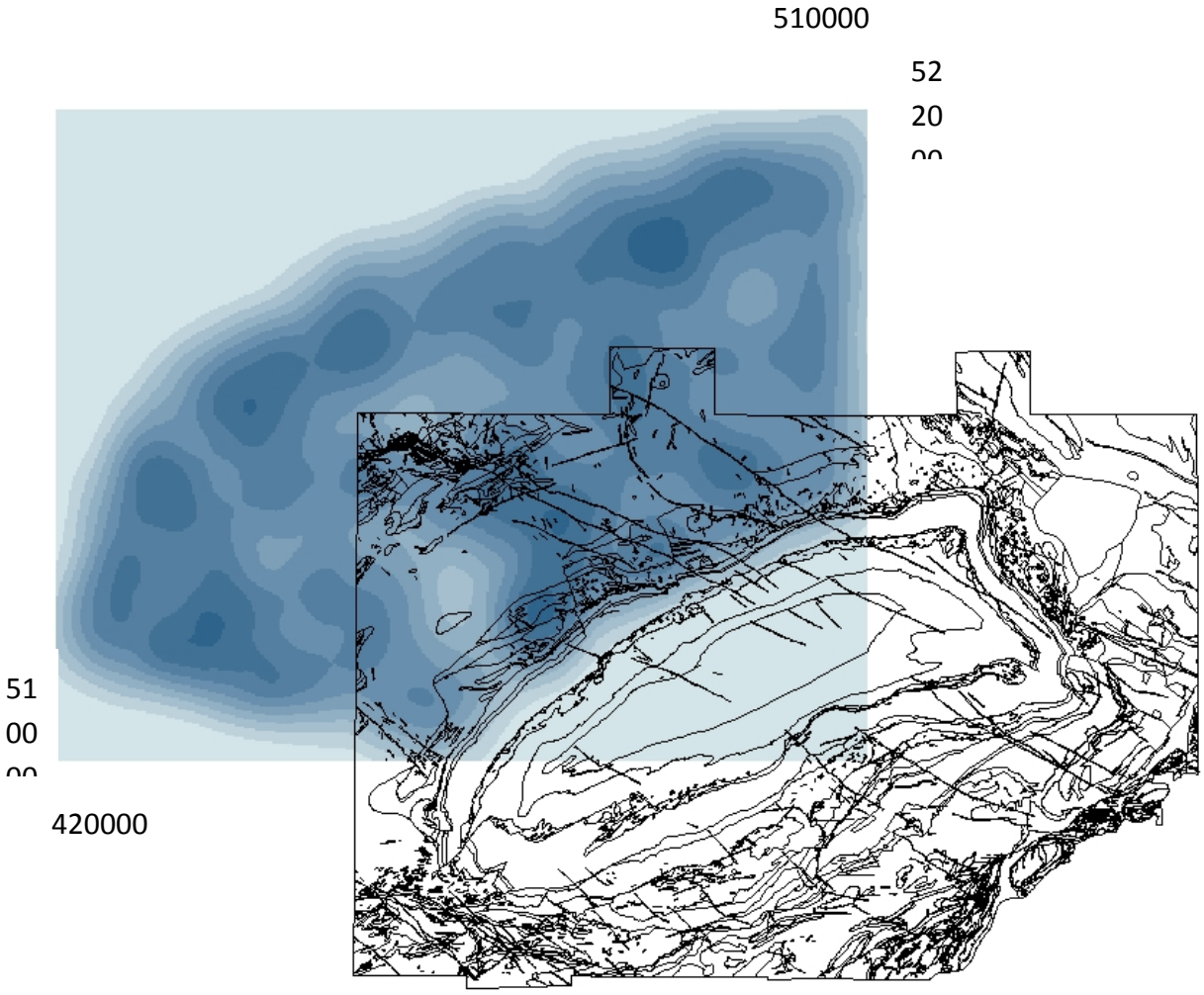

Figure 3.8

Stream flow Kernel Density at 200m cell size and 6000m kernel estimator. Geology from Ames et al (2005) has been overlaid to better visualize the correlation.

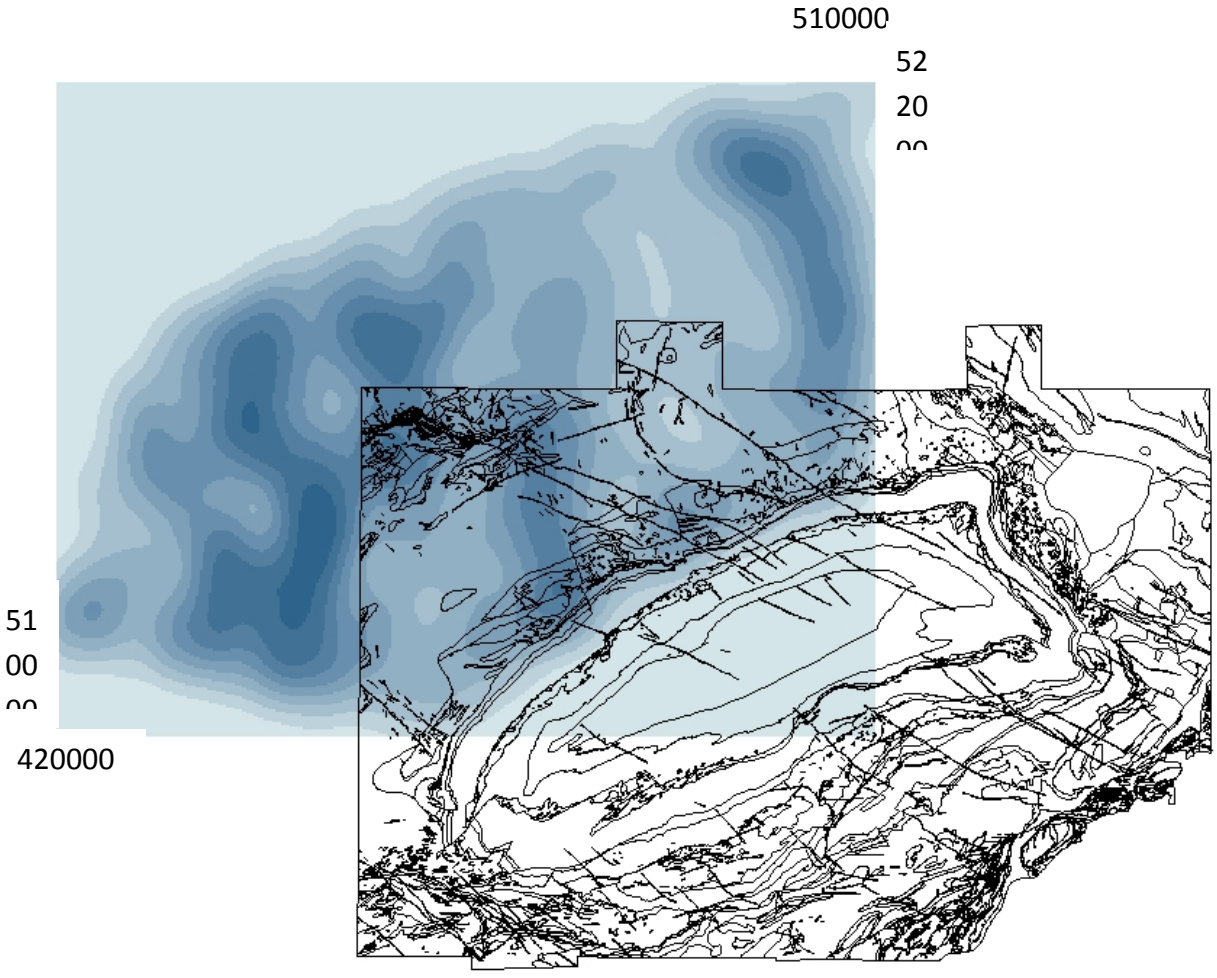

Figure 3.9

Tilt Kernel Density at 200m cell size and 6000m kernel estimator. Geology from Ames et al (2005) has been overlaid to better visualize the correlation.

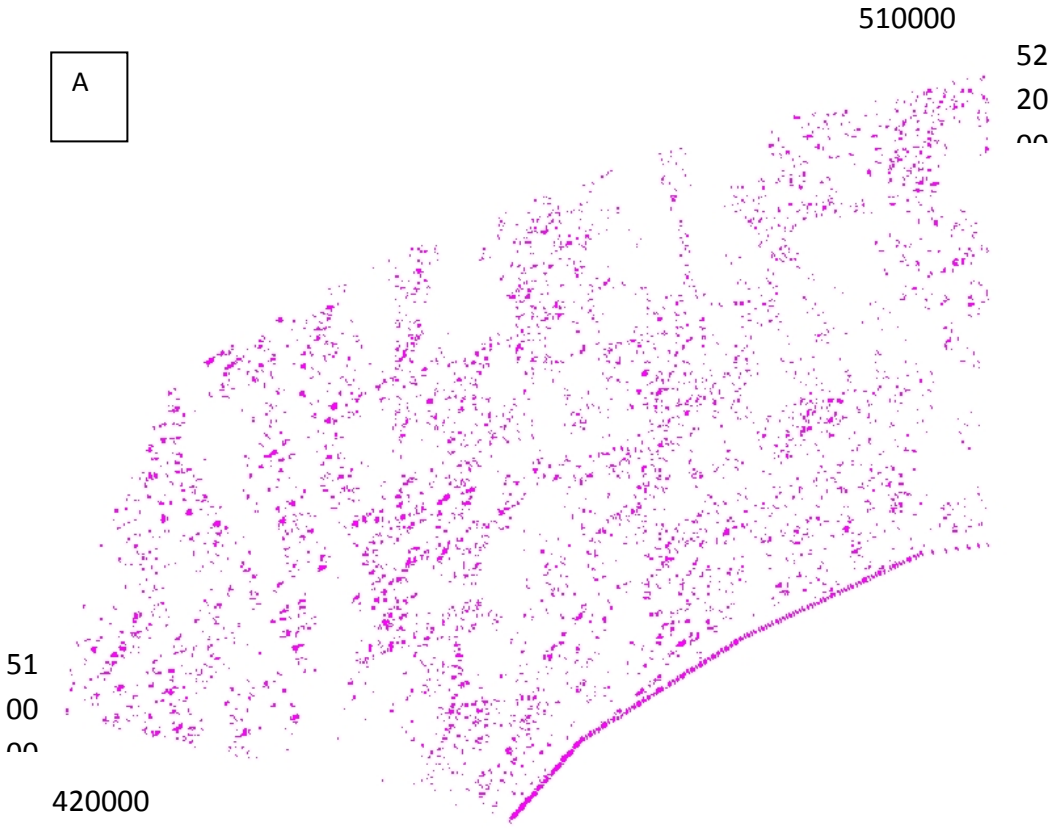

Figure 3.10

Aspect map of ASTER tilt data. Pink dots represent slopes dipping either north-west or south-east. All slopes not parallel to the SIC northern contact (bold pink line striking north-east/south-west) were removed.

Chapter 4

Syn and Post- Cratering Deformation of the Sudbury Structure

Introduction

The Sudbury Structure (SS) of north central Ontario was formed by a meteorite impact 1.84 Ga (Dietz, 1964). Based on a comparison with terrestrial and lunar impact craters, the SS would have initially had a near-circular outline in plan (Grieve, 2008). Currently, the mapped trace of the Sudbury Igneous Complex –SIC- (the impact generated melt sheet) has a near-elliptical pattern (Figure 4.1) formed primarily by two broad arcs of the North and South Range. Seismic imaging collected along a basin crossing transect as part of the Lithoprobe program suggests that the North Range, which is sitting on the Archean aged Levack Gneiss Complex (LC) dips at approximately 35^{o} to the South –East and continues at depth to the SE under the South Range (Milkereit et al., 1992, Dreuse et al., 2010; Deutsch, 1994). Geological mapping and seismic imaging reveal that the South Range has near vertical dips and is locally overturned (Riller et al., 1999). Detailed structural mapping and again seismic imagery shows that the South Range is segmented at depth by a number of sub-parallel shallow south dipping thrust surfaces collectively defined by the term South Range Shear Zone (SRSZ) (Shanks and Schwerdtner, 1991; Dubois, 2003; Riller, 2005).

Transformation of an originally near-circular crater to the current elliptical form requires deformation. Riller (1999) clearly outlined the differences between syn- and post-impact deformation. Syn-impact deformation refers to the modification of the geometrical configuration of the surrounding lithological surfaces as a direct result of the impact. Of necessity, this must be a relatively instantaneous (several minutes in duration) event which results in deformation patterns that are concentric around the impact focal point. Post-impact deformation describes modification of the crater shape as a result of later regional scale tectonic forces. There should be some continuity of the deformation from the area of the impact crater into the surrounding country rock. Since the rheological properties within and outside of the crater will be vastly different they will exhibit degrees of deformation.

The observed geometry of the SIC can be explained in two ways: (1) folding of the SIC into a south-west plunging synformal structure accompanied by northward thrusting along the South Range Shear Zone (Shanks and Schwwerdtner1999; Riller 2005); or (2) northward directed thrusting and slab rotation (Morris, 2002). If the current geometric outline of the Sudbury Structure is to be explained by folding along an NE/SW trending axis then there should

be some vestige of the folding in the rocks immediately underlying the current North Range contact. Alternatively, if the current geometry of the Sudbury Structure is explained in terms of a series of south-dipping thrust slices then there is no requirement for continuity of tectonic deformation from the area of the SIC to the surrounding region. Rather each slab could contain only syn-impact deformation which would exhibit a pattern that is coherent with the SIC contact.

The lineament analysis in Chapter 3 confirms evidence initially reported by Butler (1994) for the existence of a ring-like tectonic structure north of the basal contact of the impact crater. The presence of this ring of lineaments on the North Range of the SIC strongly supports the idea that the Sudbury Structure was formed as a multi-ring basin (Butler, 1994)). Ring-like structures can occasionally be present in smaller craters such as central peak and peak ring craters (Croft, 1981) however, they are most commonly associated with large multi-ring basins. Genesis of these basins can be of two forms; (1) several large down faulted grabens, each representing a ring, or (2) tens to hundreds of closely spaced smaller faults each representing its own ring. In both cases the geometry of the rings shows a close relationship to the geometry of the crater wall contact. The GIS analysis of fracture patterns (lineaments) reported in Chapter 3 supports Butler's (1994) original study that the ring-like structure on the North Range is sub-parallel to the SIC contact. This observation has direct implications for the presence and distribution of any post-impact deformation of the North Range. Most of the North Range footwall is formed of Archean age granites and gneisses that are incapable of providing much evidence of regional scale tectonic rotation. There are, however, a number of isolated features that are capable of being used to provide parse evidence of the degree and distribution of syn- and post-impact deformation. This study reports the results of a statistical analysis of the orientation of Matachewan diabase dikes that were intruded prior to the impact event, and Offset dykes which were intruded simultaneous with solidification of the melt-sheet. Details of the geometrical arrangement and spatial distribution of these elements are compared with paleomagnetic and tectonic data from the melt sheet to suggest that the North Range footwall has not been folded but has been modified by a series of thrust and faulting events.

Background geology

There are a number of features which indicate that the Sudbury Structure which lies on the boundary between the Archean Superior Province to the North and the Paleoproterozoic Southern Province to the South was formed as a result of a meteorite impact event (Grieve et al., 2008;, Deutsch, 1994, Kellett & Richard, 1996). The Sudbury Structure comprises the meta-sedimentary basin of the Onaping and Onwatin formations, the surrounding elliptical Sudbury Igneous Complex (SIC), and the related shocked and brecciated rocks of the Superior and Southern Provinces (Stoffler et al., 1994). The >2 km thick SIC has been dated to about 1850 Ma and has generally been accepted as the exogenic impact melt of a large scale meteor impact (Grieve et al., 2008). The slow rate of cooling of the melt sheet caused the minerals to differentiate. The lower most unit at the contact with the footwall is the inclusion rich sublayer. Its matrix is composed of fine to coarse norite to gabbro and it is host to footwall xenoliths and contains sulphide rich igneous inclusions, which also fills the radial and concentric offset dikes. Stratigraphically above the sublayer is the norite which is primarily composed of plagioclase, augite, enstatite, biotite, and amphiboles (Dubois and Benn, 2003). Quartz-gabbro gradationally overlies the norite and can be distinguished primarily by its increased quartz content. At the top of the sequence are the granophyres which grade into the overlying Onaping Formation (Dubois and Benn, 2003). The Onaping Formation is considered to be a fall back breccia although the precise mechanism of emplacement remains debated (Ames et al., 2005). At the very top of the stratigraphy are the Onwatin and the Chelmsford formations which are sedimentary rocks deposited after the basin formation (Dressler et al., 1991).

The Sudbury Igneous Complex is bound to the north and east by the Levack Gneiss Complex (LGC). Further north of the LGC lie the Archean basement rocks of the Superior Province. The rocks comprising the study area are predominantly greenstone-granites which are characterized by upright folds, dome structures and low to medium grade metamorphism of the 2.4 Ga Blezardian Orogeny (Riller, 1999). Although the Southern portion of the Sudbury Structure was deformed during the 1.85 -1.82 Ga Penokean Orogeny (Deutsch, 1994), the Archean rocks to the north remained relatively unaffected. Three swarms of intrusions transect

the study area; 2.47 Ga Matachewan dykes, 2.2 Ga Nipissing sills, and 1.24 Ga of the Sudbury dykes (Siddorn, 2002).

Matachewan dykes

The Matachewan dykes are a north to north-west trending swarm of 2.47 Ga diabase dykes which cover an area of about 250,000km^{2}in north central Ontario (Halls, 1991). They were intruded over the course of a few million years, during which time the magnetic poles reversed which caused the dikes to exhibit bimodal remanent magnetization (Siddorn, 2002). The large area in which they were emplaced has undergone differential metamorphism resulting in dykes maximally deformed to the south west (near SIC) and minimally to the north within the Kapuskasing zone (Halls, 1991). The dykes are primarily composed of plagioclase feldspar, clinopyroxene, amphibole, biotite, magnetite, and quartz (Siddorn, 2002). A key variable in dyke petrology that exists between areas with having differing metamorphic grade is the degree of clouding exhibited by the plagioclase feldspars in Matachewan dikes. This petrological variation has been interpreted in terms calcium rich plagioclase re- equilibrating with decreasing temperatures in deep crustal magmatic bodies. The degree of clouding is therefore positively proportional to the depth of emplacement (Halls, 2002). This slow cooling alteration of plagioclase results in the exsolution of clinopyroxene and magnetite, with a remanent magnetization very similar to the primary remanent direction (Halls, 2002). Hence spatial variations in the degree of clouding can be used to identify regions with differential uplift.

Offsets dykes

The Sudbury offset dykes are a series of magmatic extrusions from the slow cooling melt sheet of the 1.85 Ga impact crater (Wichman and Schulz, 1993). Their compositional similarity to the SIC Sublayer suggests they were emplaced after initial differentiation of the melt sheet had occurred (Lightfoot, 1997). They have formed in radial and concentric fractures in the country rock up to 28 km north of the north range of the current SIC (Wichman and Schulz, 1993).

Paleomagnetism

Paleomagnetism measures the inclination and declination of ancient magnetic fields embedded in rocks. It is measured as a vector oriented towards the magnetic north pole of the

time of remanence acquisition. In any magnetic body, the original remanence vector orientations should all point in the same direction. Any deformation, such as folding, will reorient these vectors into a systematic pattern of vector rotation. Using a paleomagnetic fold test, these vectors can be unrotated. If they all return to a similar orientation after unfolding, then one can assume the folding occurred after remanence acquisition. If, on the other hand, the vectors become erratic after unfolding, one can assume that they were acquired after folding (Pye et al., 1984).

Paleomagnetic studies of the Sudbury norite and Foy Offset dyke have been undertaken by Sopher (1963), Larochelle (1969), Morris et al. (1981), Morris (1982) and Szabo (2006). Combined, their data represent a thorough coverage of the SIC norite of the north range (*Figure 4.2).*

Methodology

Matachewan Dykes

As noted above, Matachewan dykes exhibit a strongly defined NNW trend in areas distal from the SS (Halls, 1991). Since emplacement of the Matachewan dykes predates formation of the Sudbury Structure these marker units are potentially capable of recording both syn- and post-impact deformation patterns.

Unfortunately, while the morphology of dykes is useful for highlighting the trajectory of a fault by continuity of common truncation points, the morphology of dykes has limited application for mapping the effect of folds. Folding about an axis oriented perpendicular to the regional trend of the dyke swarm will produce no change in dyke orientation. And depending on the degree of folding rotation about an axis parallel to the dyke trend again will not change the dyke trend but will modify the dip of the dyke. This could be measured in the field, or possibly modeled from aeromagnetic data. Neither of these two options is possible with the Matachewan data set. Finally, any rotation about a vertical axis, perhaps recorded as a fault should be clearly present in the azimuth data.

Matachewan dyke spatial distribution and azimuth data was obtained from Ames et al., 2005) map of the Sudbury Structure and its surrounding geology. The map shape file contained digitized trajectories of the Matachewan dykes. Azimuth data was obtained via hand

measurements in Geosofts Oasis montaj using the direction tool. This tool allows precise measurement of a single feature with the only error being that of measurement. In order to minimize this bias all azimuths were rounded to 5° and 10° intervals. A histogram of dyke azimuths (figure 4.4) was created to visualize the rotated proportion of the dyke population. The data was separated based on azimuth into two subsets, those trending north west and those trending north east. Each of these data sets was converted such that each dyke was represented by a single point at the center of the dyke. They were then run through a series of buffers, geometrically identical to the SIC analysis. This procedure is sensitive to deformations about horizontal fold axes. The primary limitation of the procedure is large error and limited number of observation points.

Plagioclase clouding intensity of Matachewan dykes was obtained from Siddorn (2002) using the normalized feldspar clouding intensities. In the original study Siddorn (2002) looked at the variation of clouding versus increasing distance from the SIC contact. Using this metric implies that the variation of clouding versus distance is somehow related to processes involved in the emplacement of the SIC (Siddorn, 2002). Clearly this assumption is invalid; like other studies the variation in feldspar clouding is a function of differential uplift. To address this issue we assumed that all of the data conformed to a single sheet with unknown dip direction. In this situation one can systematically vary the strike of a dipping plane and compute the correlation of plagioclase clouding versus increasing distance from the northern contact to determine the spatial relationship between dyke azimuth and distance from the SIC.

The North Range Footwall area has been eroded into a planar surface subsequent to regional deformation of the SIC (Riller, 2005). As variations in plagioclase clouding intensity record differing depth of emplacement, a record of the spatial distribution of clouding reveals deformation patterns. If similar clouding intensities conform to a single planar surface (depth of emplacement) then an optimum correlation value, as defined by a maximum $R^{2,}$ can be found and will provide an estimate of the strike of the dipping surface. Varying the orientation of the dip direction and monitoring the resulting changes in the magnitude of R^2 provides an indication of the reliability of the directional estimate.

Foy Offset

Recent exploration activity in the footwall of the North Range SIC has resulted in the acquisition of a number of aeromagnetic surveys. After leveling and microleveling each individual dataset a single compilation aeromagnetic coverage of the North Range has been developed with a grid cell resolution of 10m. The Foy Offset dyke is outlined by a distinct linear magnetic anomaly (Fig 4.3). With distance from the SIC contact the Offset trends NW-SE, becomes more E-W and then changes back to NW-SE. Further north the offset is displaced across the Sandcherry Fault. If deformation of this Offset dyke has occurred, then using the magnetic anomaly data it should be possible to detect rotations perpendicular to the trend of the Offset through inverse modeling of the associated magnetic anomaly. Accordingly a series of magnetic profiles across the Foy Offset oriented perpendicular to the local Offset trend were extracted from the magnetic compilation data set. Unconstrained 2D inversion models of the magnetic profiles were calculated using a simple dipping tabular body with Oasis Montaj's Potent. Although the magnetic anomaly associated with the Offset does have a significant remanence contribution, this does not affect the dip calculation since the remanence direction is sub-parallel to the Present Earth's Field direction. To facilitate easy visualization of the varying dip of segments of the offset, the individual block models are imaged in a single model prepared with Pitney Bowes Modelvision.

These inversion models are incapable of providing any direct information regarding rotation of portions of the Offset about WNW-ESE trending axes; parallel to the long axis the Sudbury Structure ellipsoid. Since geological mapping has suggested that the North Range is dipping to the SSE at about 40^{o} it is important to investigate any sources of information that might reveal evidence for deformation along this axis. Over the years there have been numerous paleomagnetic studies of the Sudbury Structure. Sopher (1963) and then later Larochelle (1969) have reported paleomagnetic results from the main mass of the Sudbury Igneous Complex. Later, Morris (1982) and Morris and Pay (1981) expanded the study to include samples from various sections of the Foy Offset. More recently, Szabo and Halls (2006) have reported results from breccia zones located in the North Range Footwall. Since all of these geological elements are believed to have been formed over a very short period of time they should have a similar

remanence direction. Any variation in the remanence direction thus is indicative of localized tectonic rotation.

Results

Matachewan

Due to the low number of outcrops and the discrepancy between mapped Matachewan dykes of Siddorn (2002) a certain caution must be used when interpreting the results. Histograms of dyke azimuths show nearly 180° degree range of the dyke azimuths (Figure 4.4). Using either 5° or 10° bins for the histograms serves to accentuate some of the detailed variation present in the data set. Although the trace of the histograms are slightly different, the dominant population is consistently oriented north-west with a mean direction around 320°. The 5^{o} bin histogram shows the NW peak does not have an ideal Gaussian variation; rather the distribution seems to exhibit a northerly skew. It is difficult to identify any other well-defined grouping of dike directions hints of sub-populations at about ~10° and then again at ~45° are present in the 5^{o} bin histogram.

To augment the quantification in the angular variation of dyke azimuths, another analysis was performed to study their spatial distribution. As can be seen in figure 4.5, the north west trending dykes cover the entire North Range relatively consistently, with a prominent maximum at 2km north of the SIC and a smaller population bulge from 17.5km to 22km. The north east trending dykes (figure 4.6) display a similar pattern with an obvious peak at 2km and a second population at 15km to 21km with a swath from 10km to 13.5km where there are none present. When plotted there appear to be three populations of rotated (north east trending) dykes; near the SIC to the north east, near the SIC to the west and north of the SIC by ~15km- 20km (figure 4.7).

Plagioclase clouding intensity data shows that there are best fit planar surfaces for two distinct populations; one with a dip direction of 023° (figure 4.8) from north and one with a dip direction of 0° (figure 4.9). The larger population which dips towards 23° has an R^2 of 0.5125 whereas the smaller anomalous population which dips towards 0° has a maximum R^2 of 0.9098. This indicates the significantly stronger correlation of the anomalous populations. Figure 4.10 shows the R^2 value for both populations every 5° from 0 to 180.

Both populations suggest feldspar clouding intensity decreases with increasing northerly distance, indicating that the data are describing two distinct blocks which are both dipping to the south. The bound between the two areas loosely corresponds with the edge of the Benny Deformation Zone and one of Butler's (1994) proposed impact crater related rings (130km diameter) (Figure 4.11).

Foy Offset

The magnetic inversion was completed on four profiles across the Foy Offset: the more southerly two are located east of the Sandcherry Fault, while the more northerly two profiles are west of the same fault. As noted above given the trend of the Offset, the magnetic profiles extracted across the Offset and the orientation of the fault separating the two sets of data this method is only capable of detecting any rotations about axes oriented parallel to the trend of the fault. The resulting models clearly shows that there has been a rotation in the offset dyke as there are two distinct dips to the Foy offset, a steep dip to the west close to the SIC and a steep dip to the east further from the SIC (figure 4.12).

Discussion

The large apparent variation in orientation of the Matachewan dykes is initially troubling. Studies from other adjacent areas many of which have similar lithology, indicate that Matachewan dykes intruded into Archean age metavolvanics, or gneisses exhibit a consistent north-north-west trend. Allowing for errors in extracting dike orientation from Ames et al., (2005) map, one would only expect directions variations of less than 60^{o}, that is +/- 30^{o} from the mean. There are three possibilities to account for the much broader observed variation: (1) mis-mapping of the dykes. Often individual dikes are mapped on the basis of small isolated outcrops and as such estimation of the trend of a dike may have been mistaken. (2) Mis-identification of the dike. Again when looking at a small outcrop it is difficult to differentiate between different generations of diabase dike. And (3) it is possible that some of the observed variation does genuinely reflect the effect of deformation. However, it must be remembered that rotation about an horizontal axis with any orientation can only produce a limited degree of variation in the apparent orientation of the dike since large rotations would transform the dike into a flat dipping layer. Explaining the observed azimuthal variation in terms of tectonic rotation therefore requires

that most of this rotation must have taken place about a sub-vertical axis. Logically, this suggests that if the azimuthal variance is to be explained by deformation that one should be looking for fault blocks: areas characterized by internally coherent dike azimuths having sharp bounds with adjacent areas which have a different mean dike azimuth. Such variation can be investigated by looking at the spatial distribution of individual dike azimuths.

The plagioclase clouding intensity clearly identifies two planes offset from one another. The 23° plane corresponds with the southerly dip of the Archean basement, the depth of emplacement of the dike and therefore erosion depth increases further north. The 0° plane, follows the same trend but is vertically offset to a shallower depth of emplacement. A shallower depth of emplacement juxtaposed against a deeper crustal emplacement indicates that the northerly block has been uplifted relative to the southerly block. The northerly fault block has higher plagioclase clouding values than those found in the southerly block. This suggests the southerly block has been more deeply eroded than the northerly block. Without direct calibration of the variation of plagioclase clouding versus depth it is not possible determine the magnitude of this uplift, or the degree of dip of the southerly block. Also the exact timing of this displacement is not well constrained: it clearly predates emplacement of the 1.28 Ga Sudbury olivine dikes. The currently available information is consistent with Spray's (2002) model of ring shaped down faulted blocks in the wall of an impact crater. Given the constraints imposed by the dike azimuth data these faults could not have been accompanied by any significant rotation. Unfortunately the sample size of the plagioclase clouding data set is relatively small and the distribution of observation points is limited. The southerly block of data points conform to a poorly defined planar surface. Deviation of individual points from the best fit line might be a result of poor sensitivity of the method, and differential uplift and rotation of tectonic blocks within the North Range block (as indicated by the magnetic modeling data), or even differences in the height of each sample point on the current topographic surface. With the current poor distribution of observation points it is possible that what we have approximated by a single planar surface might actually be composite of a series of sub-parallel surfaces. Finally, the available data best fits a planar surface, and do not have a better fit with a curve as might be expected for a fold model.

The magnetic inversion models of the sections of the Foy offset shows evidence for differential rotation along a N/S axis. Offset segments located to the east of the Sandcherry Fault dip to the east, while segments located to the west of the same fault dip to the west. A southerly continuation of this same fault is associated with a displacement in the SIC contact. The geometrical configuration of the lithological units at the SIC contact requires that this faulting must have occurred after the North Range of the SIC was tilted.

The paleomagnetic data agrees that there does not appear to be any evidence for folding along an E/W axis in the Superior province north of the SIC. The lineament analysis carried out in Chapter 2 along with the block rotations of Matachewan dykes suggest a faulting model for the area just north of the SIC. This supports Morris' (2002) model for brittle deformation of the crater (figure 4.13). If it had undergone ductile deformation and folded, there would be evidence for folding in the north range, of which there is none.

Conclusion

Matachewan dyke azimuth and plagioclase clouding and magnetic signal of the Foy offset dyke were used to determine the extent of post and syn impact crater deformation. This study's findings suggest that the Sudbury impact crater is a multi-ringed basin with a large down faulted block at ~25km north of the SIC. This large faulting event caused lateral rotation of some of the blocks resulting in Matachewan dykes being rotated from their original position.

The northern portion of the Foy offset dyke has been rotated. This suggests an E/W stress field which was most likely coeval with the deformation of the east range of the SIC. This later deformational event may have caused some of the Matachewan dykes in the east and north east ranges to be rotated. None of this data supports folding north of the SIC but brittle deformation instead.

References

Ames, D.E., Buckle, J., Davidson, A., and Card, K., 2005. Sudbury bedrock compilation; Geology: Geological Survey of Canada, Open File 4570, scale 1:50 000.

Butler, H. R., 1994. Lineament analysis of the Sudbury multi-ring impact Structure. Geological Society of America, Special Paper 293.

Deutsch, A., and Grieve, R.A.F., 1994. The Sudbury Structure: Constraints on its genesis from Lithoprobe results. Geophysical Research Letters, 21(10): 963-966.

Dressler, B.O., Gupta, V.K. and Muir, T.L., 1991. Chapter 15: The Sudbury Structure. In: Thurston, P.C., Williams, H.R., Sutcliffe, R.H. and Stott, G.M., Editors, 1991. *Geology of Ontario*, Ontario Geological Survey, Toronto, Special Volume, 593–625.

Dubois, A.J., and Benn, K., 2003. Structural analysis and Three-Dimensional Modeling of the Southwestern Sudbury Basin: Implications and recommendations for Mineral Exploration. Ontario Geological Survey, Open File Report 6121.

Grieve, R.A.F., Reimold, W.U., Morgan, J., Riller, U., and Pilkington, M., 2008. Observations and interpretations at Vredefort, Sudbury, and Chicxulub: Towards an empirical model of terrestrial impact basin formation. Meteoritics & Planetary Science, 43(5): 855-882.

Halls, H.C., 1991. The Matachewan dyke swarm, Canada: an early Proterozoic magnetic field reversal. Earth and Planetary Science Letters, 105: 279-292.

Halls, H.C., 2002. The nature of feldspar clouding and its paleomagnetic significance with reference to the 2.45 Ga Matachewan Dyke Swarm, Canada. EGS XXVII General Assembly, Nice, 21-26 April 2002, abstract #2889

Halls, H.C., 2009. A 100 km-long paleomagnetic traverse radial to the Sudbury Structure, Canada and its bearing on Proterozoic deformation and metamorphism of the surrounding basement. Tectonophysics, 474: 493-506.

Halls, H.C., and Palmer, H.C., 1990. The tectonic relationship of two early Proterozoic dyke swarms to the Kapuskasing Structural Zone: a paleomagnetic and petrographic study. Canadian Journal of Earth Science, 27: 87-103.

Kellett, R.L., and Rivard, B., 1996. Characterization of the Benny deformation zone, Sudbury, Ontario. Canadian Journal of Earth Science, 33: 1256-1267.

Lightfoot, P.C., Keays, R.R., Morrison, G.G., Bite, A., and Farrell, K., 1997. Geochemical relationships in the Sudbury Igneous Complex: Origin of the main mass and offset dikes. Economic Geology, 92: 289-307.

Morris, W.A., (1982). A paleomagnetic investigation of the Sudbury Offsets, Ontario, Canada, Tectonophysics, 85: 291–312.

Morris, W.A., 2002. The Sudbury Structure: A circular impact crater? Geophysical Research Letters, 29(20): 63-1 – 63-4.

Morris, W.A., and Pay, R.M., (1981). Genesis of the Foy Offset and its sulphide ores: the paleomagnetic evidence from Hess Township, Sudbury, Ontario. Econ. Geol., 76: 1895–1905.

Pye, E.G.,Naldrett, A.J, Giblin, P.E., 1984 (Ed.). The Geology and Ore Deposits of the Sudbury Structure. Ontario Geological Survey, Special Volume 1, 411-427.

Prevec, S. A., Cowan, D. R., and Cooper, G.R.J., 2005. Geophysical evidence for a pre-impact Sudbury dome, southern Superior Province, Canada. Canadian Journal of Earth Science, 42: 1-9.

Riller, U., 1999. Transpressive tectonism in the eastern Penokean orogeny Canada: Consequences for Proterozoic crustal kinematics and continental fragmentation. Precambrian Research, 93(1); 51-70.

Riller, U., 2005. Structural characteristics of the Sudbury impact structure, Canada: Impact-induced versus orogenic deformation- a review. Meteoritics & Planetary Science, 40(11): 1723-1740.

Siddorn, J.P., and Halls, H.C., 2002. Variation in plagioclase clouding intensity in Matachewan dykes: evidence for the exhumation history of the northern margin of the Sudbury Igneous Complex. Canadian Journal of Earth Science, 39: 933-942.

Sopher, S. R. 1963**.** Palaeomagnetic study of the Sudbury irruptive. Geol. Surv. Can. Bull. 90**.**

Spray, J. G., Butler, H. R., and Thompson, M. L., 2004. Tectonic influences on the morphometry of the Sudbury impact structure: Implications for terrestrial cratering and modeling. Meteoritics and Planetary Science, 34(2): 287-301.

Stoffler, D., Deutsch, A., Avermann, M., Bischoff, L., Brockmeyer, P., Buhl, D., Lakomy, R., and Muller-Mohr, V., 1994. The formation of the Sudbury, Canada: Remnant of the only multi-ring (?) impact basin on Earth (abstract). Meteoritics, 24: 328.

Szabó, E., and Halls, H.C., 2006. Deformation of the Sudbury structure: paleomagnetic evidence from the Sudbury breccia. Precambrian Res., 150: 27–48.

Turtle, E.P., Pierazzo, E., Collins, G.S., Osinski, G.R., Melosh, H.J., Morgan, J.V., and Reimold, W.U., 2005. Impact Structures: What does crater diameter mean? Geological Society of America, Special Paper 384.

Wichman, R.W., and Schultz, P.H., 1993. Floor-fractured crater models of the Sudbury Structure, Canada: Implications for initial crater size and crater modification. Meteoritics, 28: 222-231.

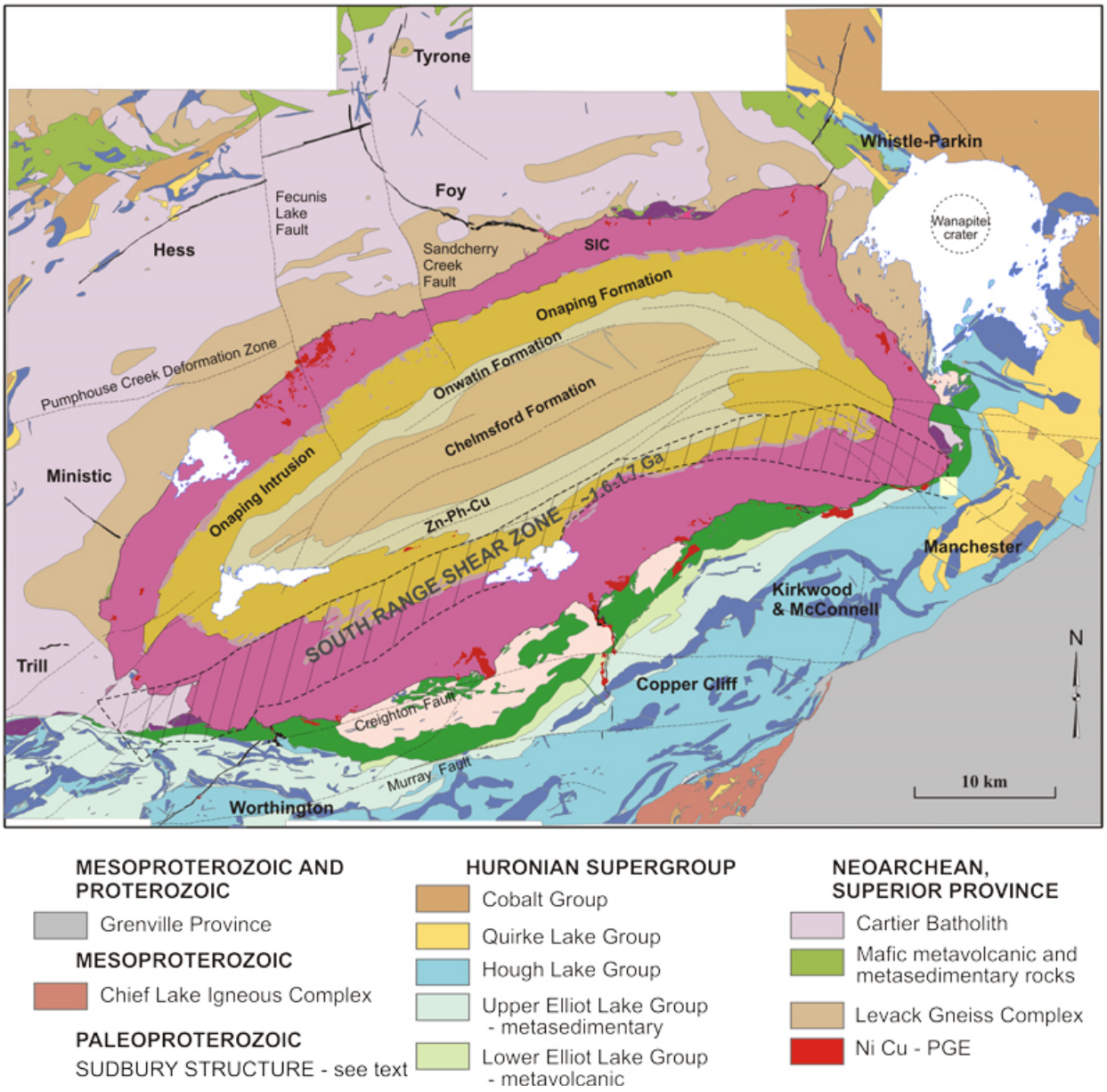

Figure 4.1

Geological map of the study area created by Ames et. al, (2005). This map highlights the Foy offset dyke and some of the large faults in the area.

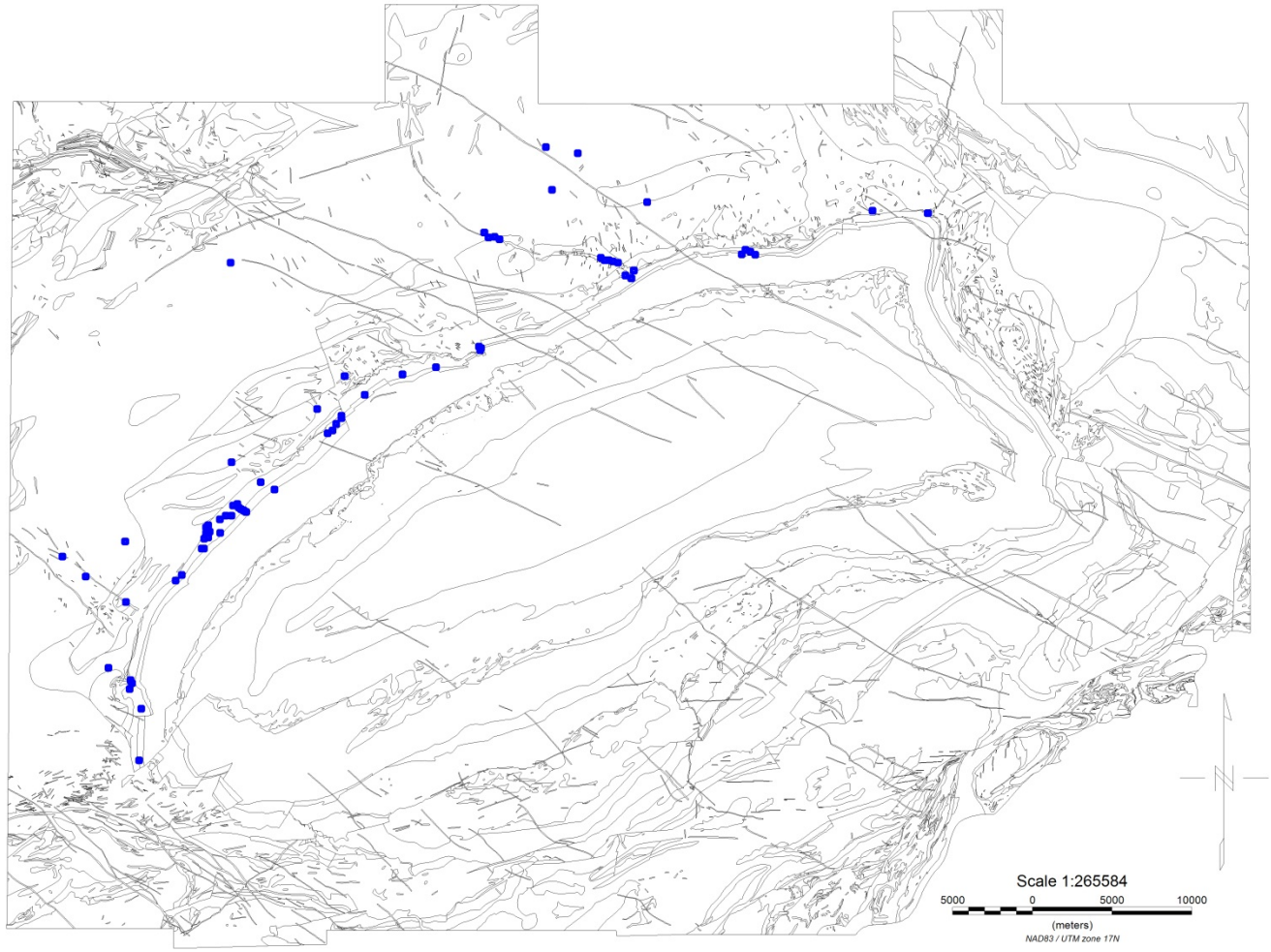

Figure 4.2

Distribution of paleomagnetic sample points (Morris et al., 1981, Morris, 1982, Larochelle, 1969; Szabo,2006; Sopher 1961)

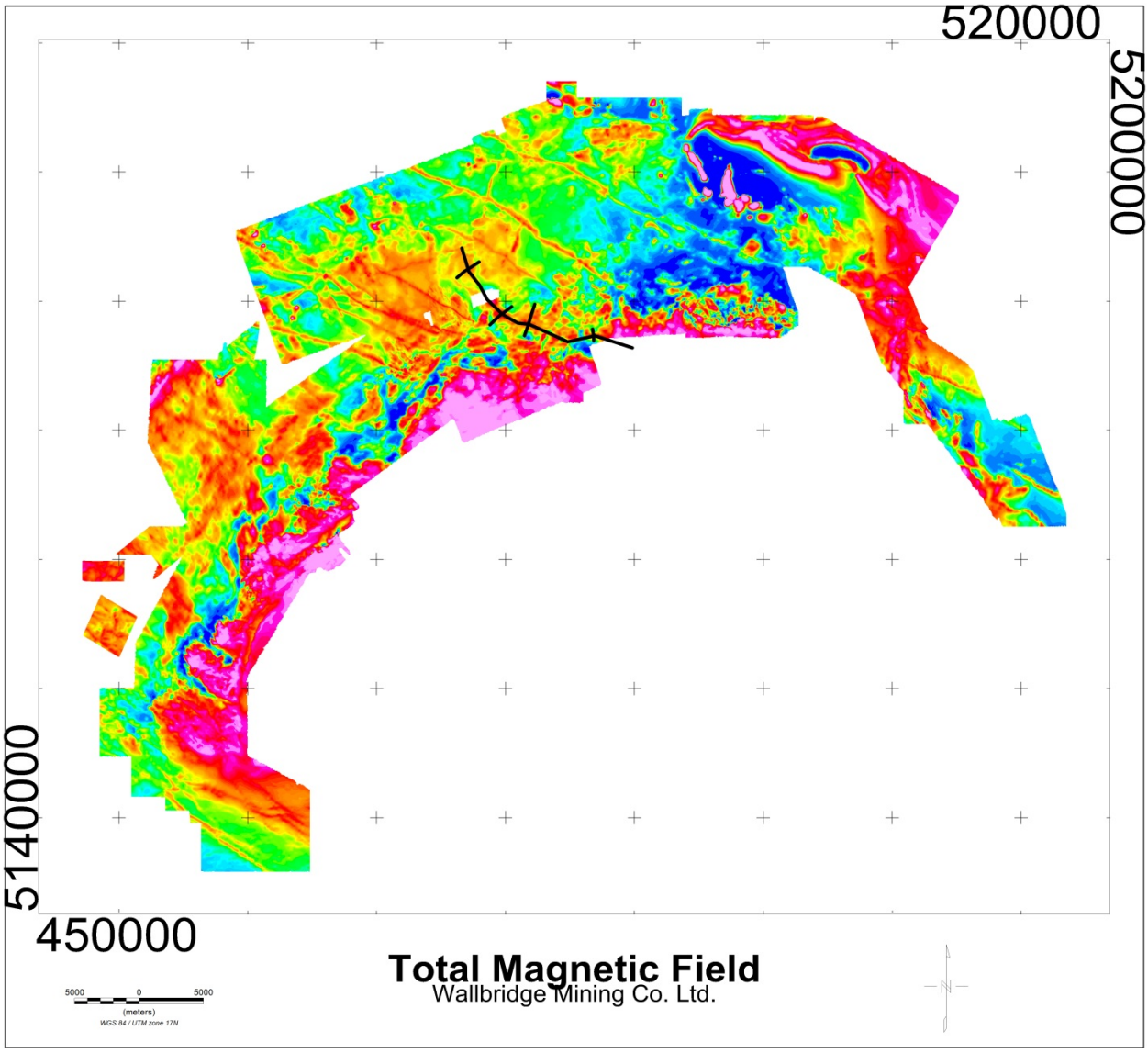

Figure 4.3

Total Magnetic Field of north range of the Sudbury Igneous Complex collected by Wallbridge Mining Co. Ltd. Resolution of 10m. Outline of the Foy Offset is marked by black line; the profiles modeled using Potent are signified by crossing short black lines.

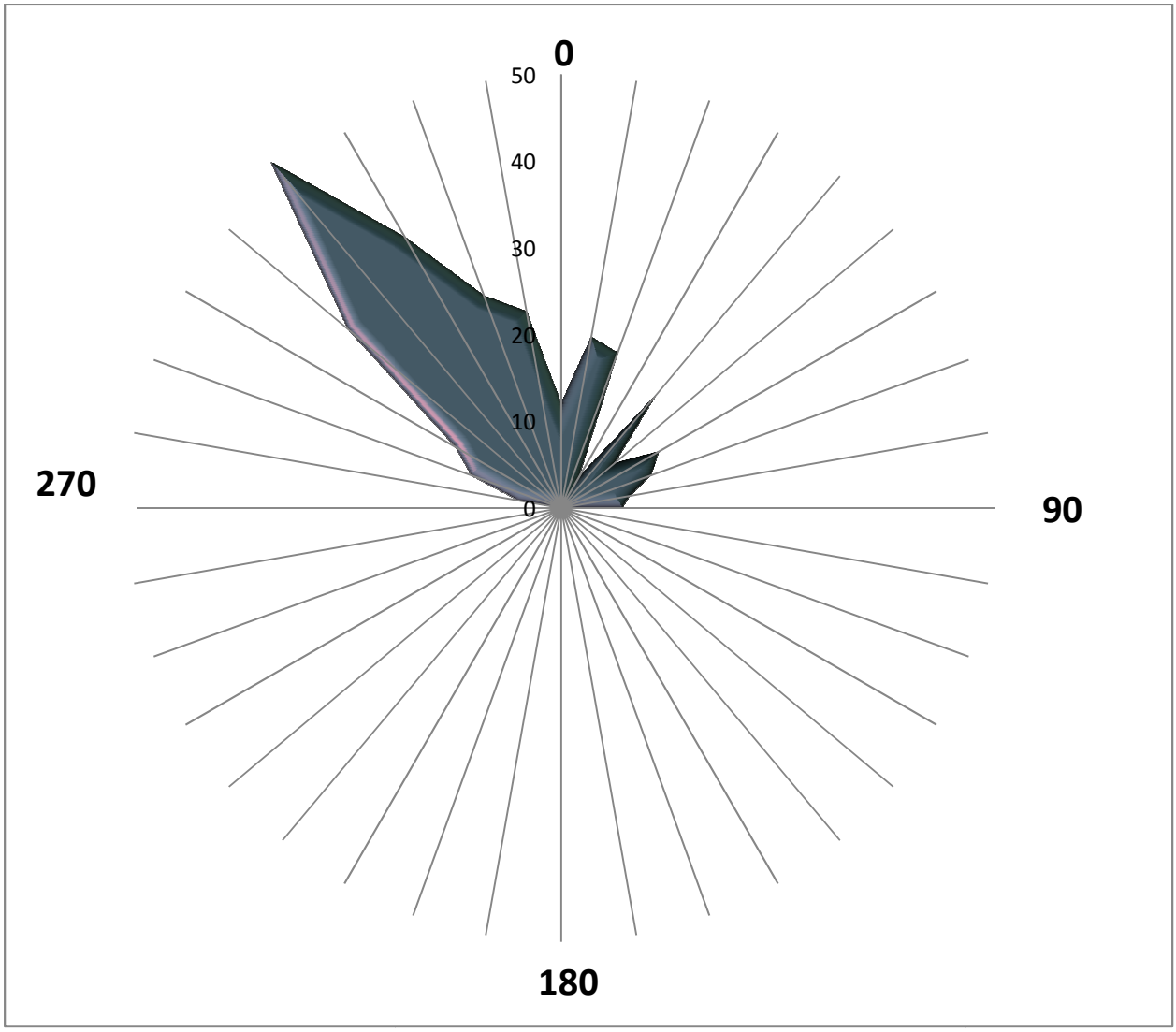

Figure 4.4

Distribution of Matachewan dyke azimuths from 0° (North) to 359°.

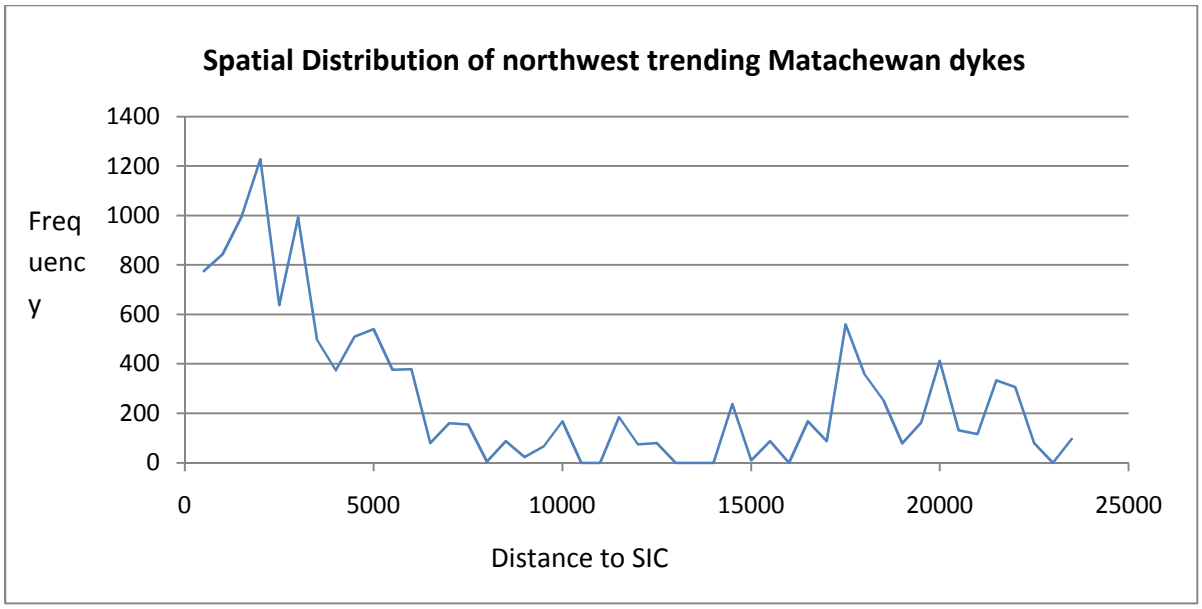

Figure 4.5

Buffering analysis of NW (non rotated) Matachewan dykes.

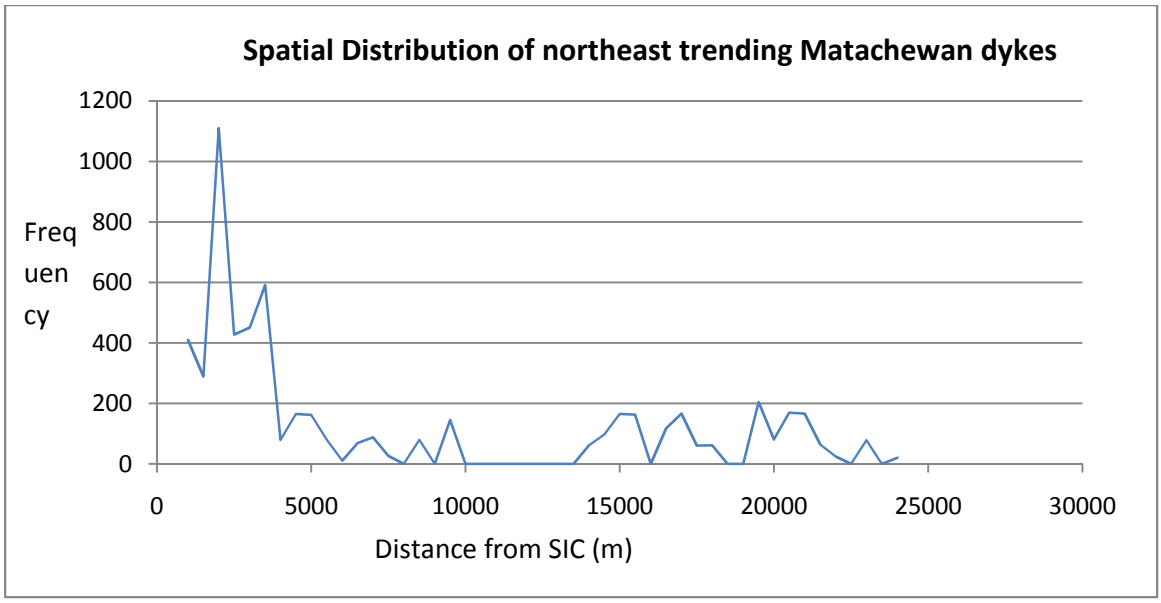

Figure 4.6

Buffering analysis of NE (rotated) Matachewan dykes.

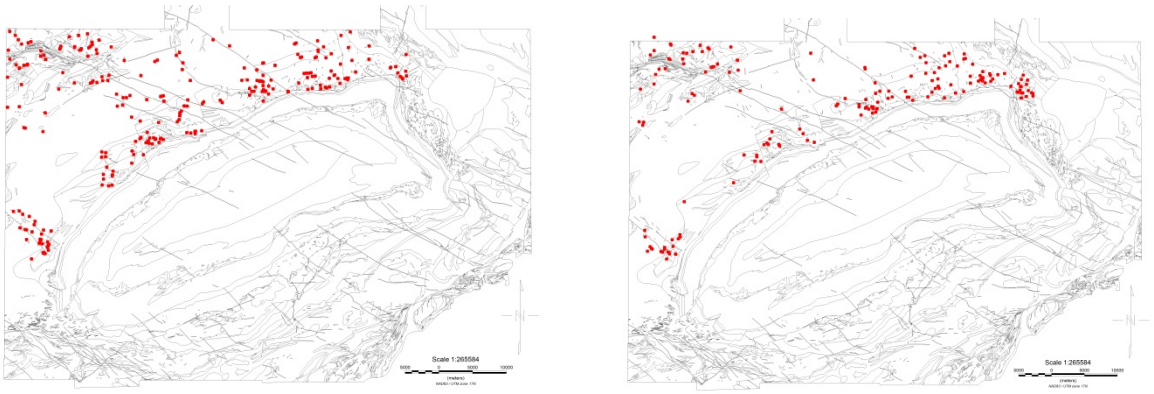

Figure 4.7

Plot of Matachwan dyke orientations, taken at the center point of dyke. (A) north-west trending Matachewan dykes, (B) north-east trending Matachewan dykes.

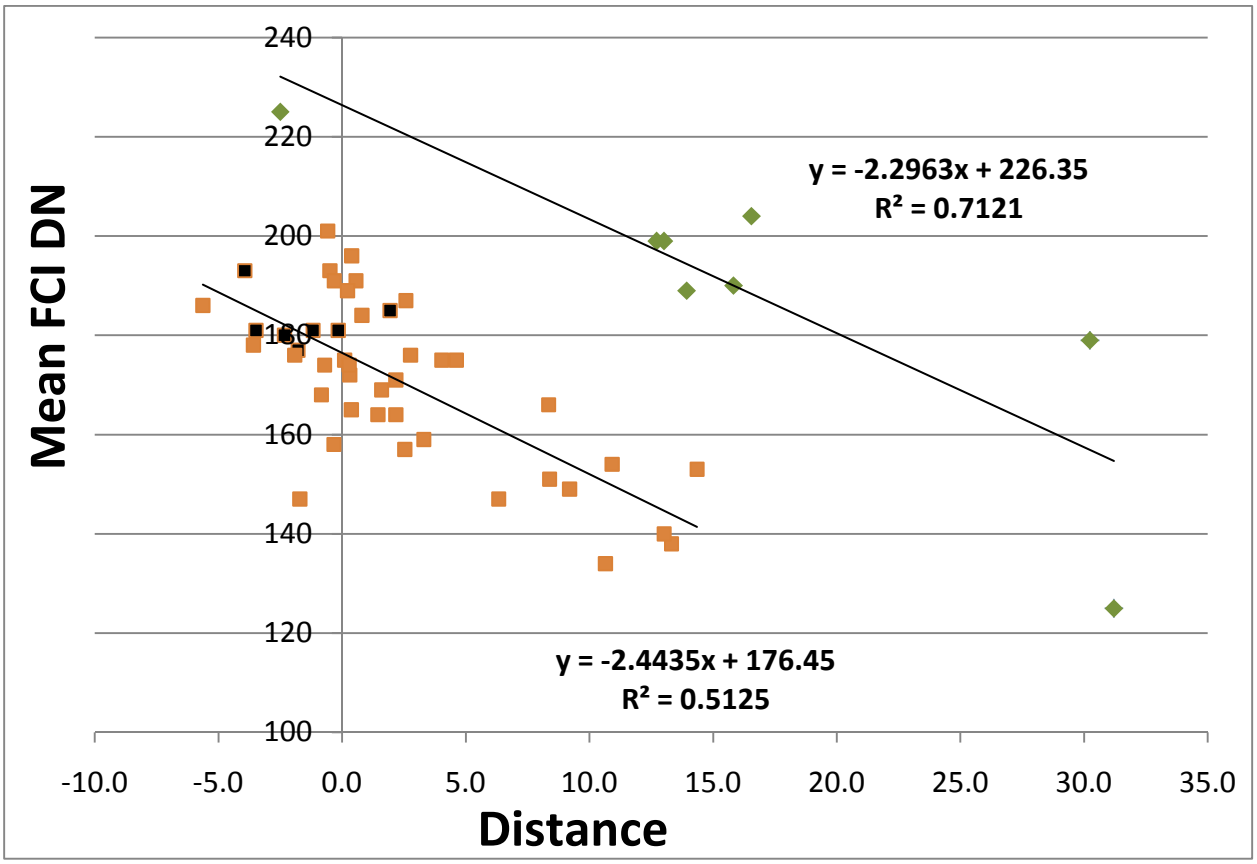

Figure 4.8

Plagioclase clouding intensity versus map distance from an arbitrary point outside of the study area. The R^2 values show a distinct grouping of two populations. The population with R^2 of 0.5125 is at its optimal orientation of 23° from north.

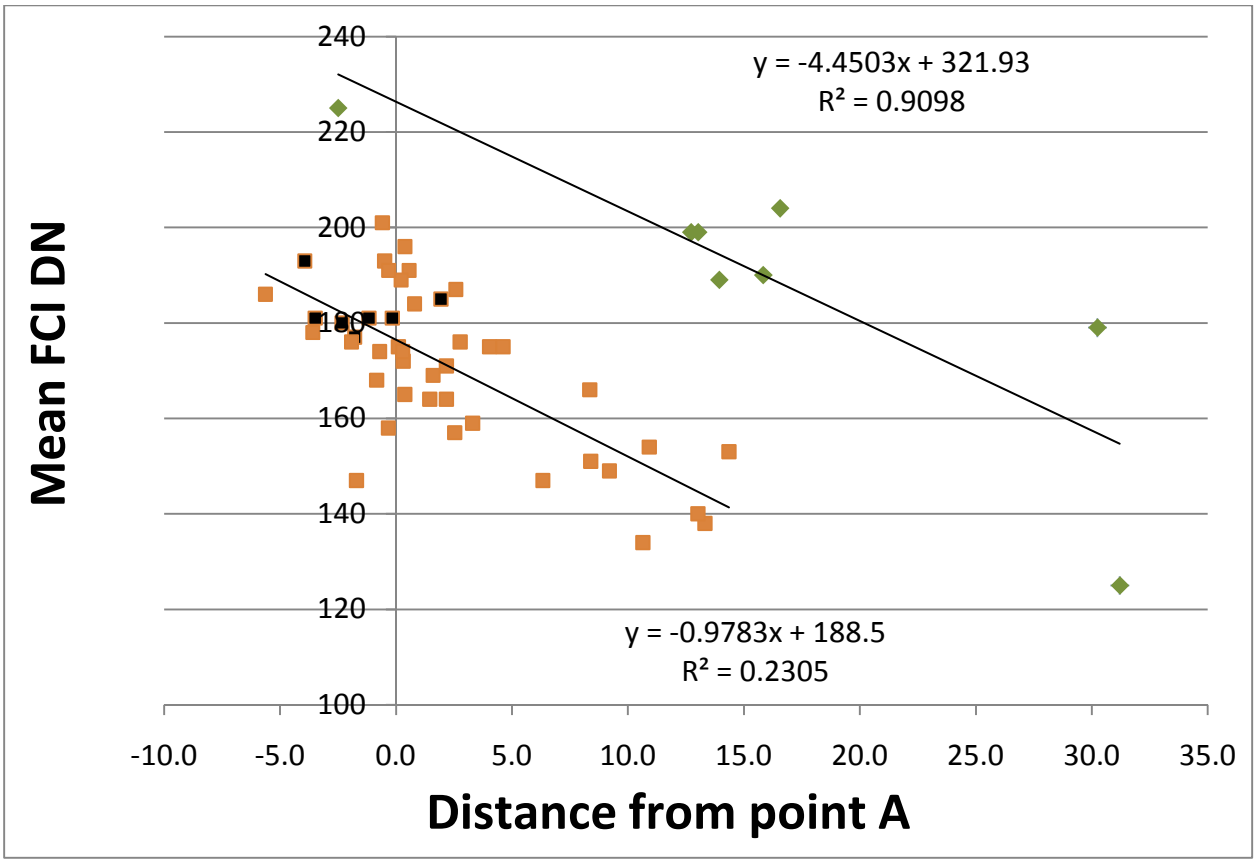

Figure 4.9

Plagioclase clouding intensity versus distance from an arbitrary point outside of the study area. The R^2 values show a distinct grouping of two populations. The population with R^2 of 0.9098 is at its optimal orientation of 0° from north.

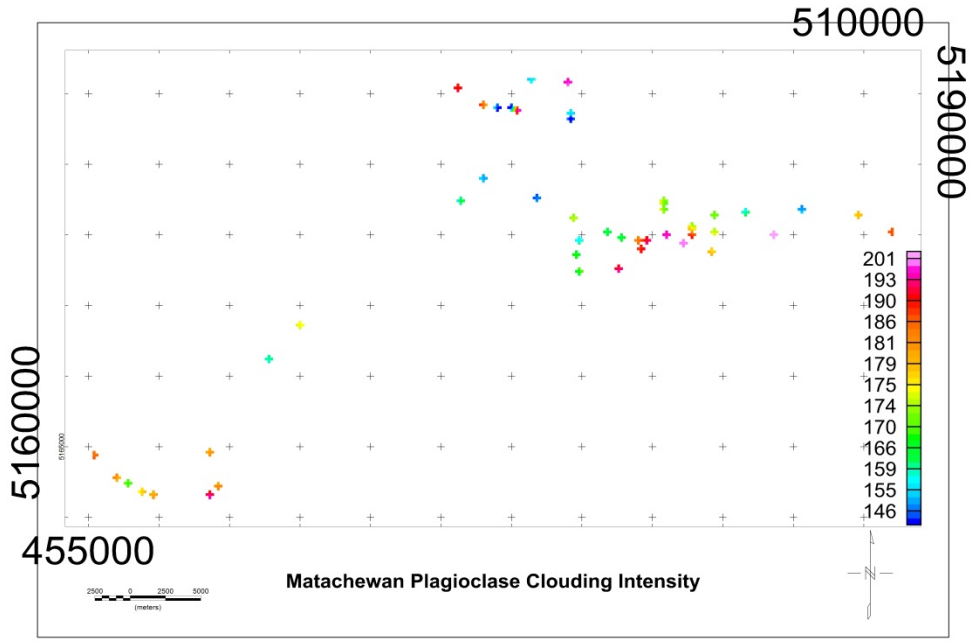

Figure 4.10

Plagioclase clouding intensities spatially plotted in Geosoft Oasis montaj.

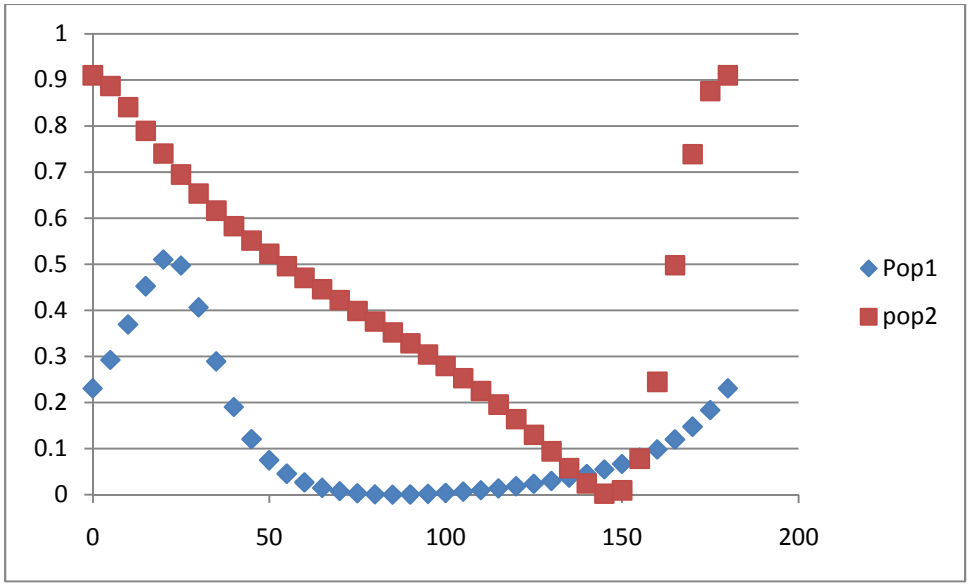

Figure 4.11

Dip directions for the two surfaces in figure 4.8 & 4.9. 180° distribution of possible surfaces shows the optimal dip direction. This demonstrates the inability to determine the exact dip direction, but instead one of two dip directions (+/- 180°).

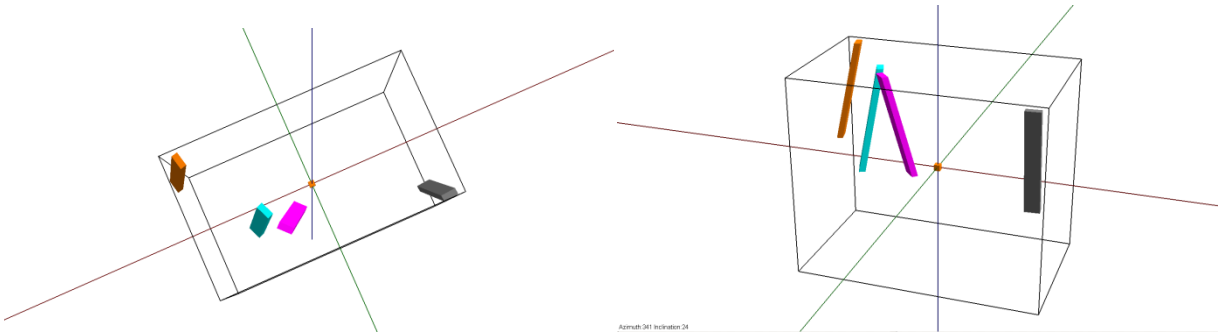

Figure 4.12

ModelVision 3D view of Foy Offset rotation. Each block represents a portion of the Foy offset where a magnetic profile was extracted. This was achieved using an unconstrained magnetic inversion in Geosofts Potent.

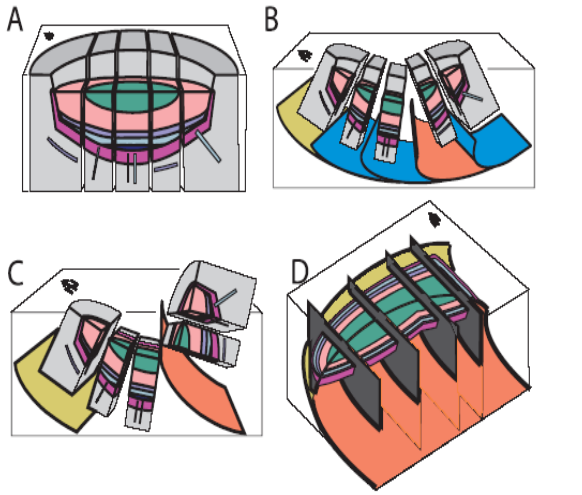

Figure 4.13

Brittle deformation model of the Sudbury impact crater (Morris, 2002).

Chapter 5

Conclusion

Matachewan dyke azimuth, plagioclase clouding, the total magnetic field signal of the Foy offset dyke and a lineament analysis of the study area were used to determine the extent of post and syn impact crater deformation. The results suggest that there are topographically significant features which geometrically mimic the northern basal contact of the SIC. The location of one these topographic anomalies align with the third ring found in Butler's (1994) study. The correlation of these two anomalies is strong evidence for the presence of a ring structure. To further increase the reliability of this finding, both the azimuths and the plagioclase clouding intensities of the Matachewan dykes support the presence of a ring. The spatial distribution of plagioclase clouding intensity suggests there are two distinct surfaces within the study area. One corresponds to the trend found by Siddorn (2002), which has a generally increasing depth of emplacement to the north, suggesting a strike of the Archean rocks to the east. The other surface is located at the same distance as the ring feature. It has a similar trend but is offset, representing a shallower depth of emplacement.

All evidence suggests that the Sudbury impact crater is a multi-ringed basin with a large down faulted block at ~25km north of the SIC. This large faulting event may have caused lateral rotation of some of the blocks resulting in Matachewan dykes being rotated from their original position.

The rotation of the northern portion of the Foy offset dyke suggests an E/W stress field which was most likely coeval with the deformation of the east range of the SIC. This later deformational event may have caused some of the Matachewan dykes in the east and north east ranges to be rotated. None of this data supports folding north of the SIC but brittle deformation instead.

Field studies should be conducted to verify many of the results obtained in this study. Direction of fault slip on the basin ring structure, composition of rotated Matachewan dykes and plagioclase clouding data should be acquired from many more Matachewan dykes, especially in the area surrounding the hypothesized ring, about 25 km north of the SIC basal contact.